

Fast Inflow Directly Feeding Black Hole Accretion Disk in Quasars

Hongyan Zhou^{1,2,3}, Xiheng Shi^{1,2}, Weimin Yuan^{4,5}, Lei Hao⁶, Xiangjun Chen^{2,3}, Jian Ge⁷, Tuo Ji^{1,2}, Peng Jiang^{1,2}, Ge Li^{2,3}, Bifang Liu^{4,5}, Guilin Liu^{2,3}, Wenjuan Liu^{8,9}, Honglin Lu^{2,3}, Xiang Pan^{1,2}, Juntai Shen⁶, Xinwen Shu¹⁰, Luming Sun^{2,3}, Qiguo Tian^{1,2}, Huiyuan Wang^{2,3}, Tinggui Wang^{2,3}, Shengmiao Wu^{1,2}, Chenwei Yang^{1,2}, Shaohua Zhang^{1,2} & Zhihao Zhong^{2,3}

¹Antarctic Astronomy Research Division, Key Laboratory for Polar Science of the State Oceanic Administration, Polar Research Institute of China, Shanghai, China

²School of Astronomy and Space Sciences, University of Science and Technology of China, Hefei, China

³Key Laboratory for Research in Galaxies and Cosmology of Chinese Academy of Sciences, Department of Astronomy, University of Science and Technology of China, Hefei, China

⁴National Astronomical Observatories of China, Chinese Academy of Sciences, Beijing, China

⁵School of Astronomy and Space Science, University of Chinese Academy of Sciences, Beijing, China

⁶Shanghai Astronomical Observatory, Chinese Academy of Sciences, Shanghai, China

⁷Department of Astronomy, University of Florida, Bryant Space Science Center, Gainesville, FL, USA

⁸Yunnan Observatories, Chinese Academy of Sciences, Kunming, China

⁹Key Laboratory for the Structure and Evolution of Celestial Objects, Chinese Academy of Sciences, Kunming, China

¹⁰Department of Physics, Anhui Normal University, Wuhu, China

Quasars are high-luminosity active galactic nuclei believed to be powered by accretion of interstellar matter onto a super-massive black hole (SMBH) therein. Most of the observed energy is released in an accretion disk of inspiralling gas surrounding the SMBH. An enormous amount of fueling material, up to several tens solar masses per year, is expected to be transported inwards and consumed in the end. However, basic questions remain unanswered as to whether and how the accretion disks are supplied with external gas, since no disk-feeding inflow has hitherto been observed clearly. Here we report the discovery of highly redshifted broad absorption lines arising from neutral hydrogen and helium atoms in a small sample of quasars. Their absorption troughs show a broad range of Doppler velocities from zero extending continuously inward up to as high as $\sim 5,000 \text{ km s}^{-1}$, comparable to the free-fall speeds close to the SMBH and constraining the fastest in-falling gas to be within 10^4 gravitational radii. We thus see through streams of cold gas moving with a radially inward velocity component that spans an immense gradient—a result of gravitational acceleration by the central SMBH. Extensive photo-ionization modeling for the archetypical object SDSS J103516.20+142200.6 indicates the inflowing gas to be dense, thick and moderately ionized, with a characteristic distance to the SMBH of $\sim 1,000$ gravitational radii, possibly overlapping or close to the outer accretion disk. Our results present the first compelling evidence for the long-sought inflow directly feeding quasars' accretion disks with external materials, likely originating from the dusty torus at a parsec scale. Our approach provides a new tool to probe the bulk of the so far elusive fueling inflows in quasars. Their studies may help address some of the fundamental questions concerning accretion physics, the onset and sustainment of quasar activity, and the SMBH growth at centers of most galaxies.

Being the most luminous steady beacons known in the universe, quasars have been a long-standing enigma in modern astrophysics since their discovery[1]. They are believed to be powered by the gravitational potential energy of accreted matter falling onto a SMBH with mass ranging from $M_{\bullet} \sim 10^6$ to $10^{10} M_{\odot}$ at centers of galaxies. The energy release takes place within an accretion disk of inspiralling gas in the close vicinity of the SMBH extending out to a few 10^{2-3} gravitational radii ($R_g \equiv GM_{\bullet}/c^2$). The observed energetics require a substantial supply of mass accretion from a fraction to several tens of solar masses per year[2]. Despite the success of this paradigm since its first clear putting forward half a century ago[3], fundamental questions remain unanswered: whether and how the accretion disks are supplied with external gas? The answers are essential for understanding further questions as to what sets off, maintains, and terminates the quasar activity and how long the quasar phase lasts for[4]. However, such an inflow directly supplying the bulk of the material required to feed the accretion disks (termed disk-feeding inflow hereafter), and subsequently the SMBHs, has never hitherto been observed clearly, albeit some controversial attempts in previous studies[5, 6].

Atomic absorption lines imprinted on the observed spectra of quasars are a robust probe of the dynamics and physical conditions of gas along the line of sight (LOS) to the central radiation source. In the optical–ultraviolet spectra of some $\sim 15\%$ quasars, broad absorption lines (BALs) with velocity dispersions $\gtrsim 2,000 \text{ km s}^{-1}$ by definition have long been observed, which are mostly produced by resonant transitions of alkaline-like metals including NV, CIV, SiIV, AlIII and MgII[7]. However, their ubiquitous blueshifts (with respect to the quasar systemic redshift) indicate outflows, rather than inflows, intrinsic to the quasar central engine[8]. Only recently BALs of metal ions showing both blueshifted and redshifted components have been observed in a handful of quasars[9]. Nevertheless, it is not yet clear to connect them to disk-feeding inflows, given the large uncertainties in the quasar systemic redshifts (several times $10^{2-3} \text{ km s}^{-1}$, as estimated from high-ionization broad emission lines) and a lacking of other evidence. In fact, metal BALs are of little diagnostic value in probing cold and dense gas with high column densities (subject to serious saturation and line blending effects; see **Method** for details), which are thought to be most probably the case of disk-feeding inflows[10], if existing.

Motivated by the fundamental questions above, we have developed a novel approach to diagnosing dense BAL gas of high column densities and low/moderate ionization, based on extensive studies of our own[11–15] and other teams[16, 17]. The approach makes use of BALs of two new atomic series that became to know in quasar studies mostly in recent years: the Balmer lines of neutral hydrogen ($H_{n+2} \equiv H_{\dots,\zeta,\dots,\alpha} \lambda \lambda \dots$, 3890, ..., 6564) and the multiplets of neutral helium He I_n^* ($\text{He I}_{\dots,3,2,1}^* \lambda \lambda \dots$, 3189, 3889, 10830) arising from transitions from the highly meta-stable 2^3S level. The Balmer lines are mostly populated by collisional excitation in the neutral zone of dense gas clouds/flows (with a density $n_{\text{H}} \gtrsim 10^6 \text{ cm}^{-3}$), while the helium multiples populated via recombination of He^+ ions. The relative abundances of H_{n+2} and He I_n^* are so low that some of their weak member lines remain unsaturated even for Compton thick absorbers. Since these line series are produced by transitions from the same low energy level but with diverse oscillator strengths, we can decouple the covering factor and column density in modeling the lines. The Balmer lines depend on both the ionization and density, while the He lines are sensitive almost solely to the ionization parameter[18]. We can therefore break the degeneracy of the ionization and density by

joint analysis of the two line series. Lastly, the wide spaces in wavelength between the member lines relieve the line-blending effect—a problem often encountered in metal BALs.

In our ongoing program of systematic search for redshifted BALs of both H_{n+2} and $He I_n^*$, we discovered eight such objects from $\sim 10^5$ quasars at redshifts $z < 1.3$ in the Sloan Digital Sky Survey (SDSS) spectral database of the latest fourteenth data release (DR14)[19]. We also obtained high signal-to-noise optical and near-infrared spectra for SDSS J103516.20+142200.6 (hereafter J1035+1422)—the archetype of the sample—and several others via observations with the Paloma 200-inch telescope and the Keck II 10-meter telescope, as well as from the VLT/X-shooter spectral archive. The combined spectrum and the BALs resulting from the analysis (see **Method**) for J1035+1422 are presented in Figure 1 and 2, while those for the remaining seven quasars in Extended Data Fig. 3 and 4 in **Method**. Although the H_{n+2} BALs are superimposed on the corresponding broad emission lines (BELs), we could disentangle one from another by taking advantage of the Balmer decrements. We also detected redshifted BALs of $He I_{1-3}^*$, after removing the H_ζ BAL component. The redshifted BAL troughs of H_{n+2} and $He I_n^*$ in the same objects show a largely common Doppler velocity structure starting from $v \sim 0$ and extending continuously up to a maximum velocity that falls within $v_{\max} \sim 3,000 - 5,000 \text{ km s}^{-1}$ in five objects while $v_{\max} \sim 1,000 - 1,500 \text{ km s}^{-1}$ in the remaining three (thus classified as mini-BAL traditionally).

These detections are unprecedented. The lines are highly Doppler-redshifted and broadened by radially inward motion of the absorbing gas with a large velocity gradient projected along the LOS toward the central continuum source (nearly toward the SMBH). This indicates that we are seeing through continuous streams of gases that are transported inward to the central engine. The large maximum BAL velocities measured are remarkable, being one order of magnitude larger than those of starburst-driven outflows and winds of other stellar processes[22], suggesting the association with the central engine. Since the radial velocity cannot exceed the free-fall speed of the gravitational acceleration due to the central SMBH, $v_{\max} < v_{\text{ff}}(R) = \sqrt{2GM_\bullet/R}$ (from infinity), we can constrain the distance of the innermost gas to the SMBH as $R < 2GM_\bullet/v_{\max}^2 = 2R_g(c/v_{\max})^2$. For the majority of the sample we have $R \lesssim 10^4 R_g$, well within the sphere of influence of the central black hole at the order of $\sim 10^6 R_g$ scale. Specifically for J1035+1422, $R \lesssim 7,200 R_g$. The distance limit would become even smaller if the kinematics of the gas deviates from sole free-fall motion (e.g. subject to a centrifugal force due to sub-Keplerian motion and/or strong radiation pressure from the central source), or there exists even faster infalling part of the inflow not intersecting the LOS. Inevitably, to gain such high radial velocities, the gases must be experiencing gravitational acceleration by the central SMBH. The large velocity gradient suggests that the LOS intersects a large number of (most likely inspiralling) streams at various radii across a wide radial distance, starting from somewhere at larger radii and ending much closer inside.

In the rest of this paper, we performed further detailed analysis for J1035+1422 ($z = 1.2528 \pm 0.0001$) as demonstration, which has the highest data quality among the sample. The quasar has a mass accretion rate $\dot{M}_\odot \approx 13 M_\odot \text{ yr}^{-1}$ derived from its luminosity using the standard bolometric correction ($L_{\text{bol}} \simeq 8.1 L_{5100}$)[20] assuming an accretion efficiency $\eta = 0.1$, and a size of the broad emission line region (BELR) $R_{\text{BELR}} \approx 0.33 \text{ pc}$ derived from the R_{BELR} –luminosity relation[20]. We estimated the black hole mass $M_\bullet \approx 2 \times 10^{10} M_\odot$ from the parameters of the reconstructed

Balmer BEL and the size of the BELR, with an uncertainty of ~ 0.5 dex[21]. This leads to a gravitational radius $R_g \approx 9.8 \times 10^{-4}$ pc and an Eddington ratio $\eta \equiv L_{\text{bol}}/L_{\text{Edd}} \approx 0.03$.

Redshifted BAL troughs of metal ions (including CIV, Al III, Mg II, and resonant and excited Fe II) were also found in the UV part of the spectrum, showing similar velocity structures to those of H_{n+2} and He I $_n^*$ (Figure 2; see also Extended Data Fig. 7 and 8 in **Method**). These metal BALs show an additional blueshift component that is ubiquitously seen in normal BAL quasars. A similar blueshift component is also seen in the He I $_1^*$ BAL. This indicates the co-existence of an outflow with the inflow. Surprisingly, the redshift component of the CIV BAL is much weaker in strength than those of the H α and Mg II BAL. This is in contrast to what is commonly observed in typical quasar (blueshifted) BALs^{1†}, and can well be explained if the central ionizing radiation is filtered prior to illuminating the inflow gas, naturally by the blueshifted BAL outflow.

We measured the covering factor $C_f(v)$ and the column densities of $n = 2$ neutral hydrogen $N_{\text{HI}(n=2)}(v)$ and further of 2 ^3S neutral Helium $N_{\text{HeI}^*(2\ ^3\text{S})}(v)$ ($\propto N_{\text{HI}(n=2)}(v)$) as a function of velocity. To constrain the physical properties of the inflow, we performed extensive photo-ionization simulations and compared the results with the redshifted BAL spectra observed (see **Method** for details). The best-fit model indicates that the inflow gas is relatively dense, thick and moderately ionized (a density $\log n_{\text{H}} = 7.20_{-0.45}^{+0.40}$ cm $^{-3}$, a total H column density $\log N_{\text{H}} = 23.46_{-0.24}^{+0.33}$ cm $^{-2}$ and an ionization parameter $\log U = -0.24_{-0.64}^{+0.06}$ at the 90% confidence level). We found the most probable characteristic distance of the inflow to the SMBH, as represented by the optical depth-weighted distance, to be $R_{\text{IF}} = 1.01_{-0.50}^{+2.16}$ pc (Figure 3, see also Extended Data Fig. 6 in **Method**). The distance corresponds to $R_{\text{IF}} \simeq 525 - 3,236 R_g$, complying with the above upper limit constrained by the simple physics of gravity. It is worth noting that, albeit large uncertainties, the inner inflow has an inferred radial distance comparable to the outer radius of the accretion disk in J1035+1422, which we estimated to be from a few hundred to about one thousand gravitational radii. The actual innermost end of the downstream may be at even smaller radii if it deviates from—and does not intersect—the line of sight. We calculated the force exerted on the gas by the central radiation to be only 1 – 2% of the black hole’s gravity. Hence the dynamics of the inflow gas is dominated by the SMBH.

These properties leave little room for the other destinies of the inflow but the one as the following. The bulk of the inflow downstream would mostly be gravitationally pulled onto a general plane defined by the overall angular momentum, as depicted in Figure 4. Ultimately, the materials transported therein by the inflow are likely somehow dumped into the outer accretion disk and/or the marginally unstable region extending further out. Assuming an axial symmetric geometry on the general plane for the global inflow, we estimated a total mass inflowing rate from the above derived total column density, $\dot{M}_{\text{IF}} \sim 30 M_{\odot} \text{ yr}^{-1}$ (see **Method**). This is sufficient to power the quasar radiation luminosity observed ($\sim 13 M_{\odot} \text{ yr}^{-1}$), and likely the outflow as well. We thus consider the redshifted BALs in J1035+1422, and in other quasars of our sample in general, to be compelling

^{1†}For any gas directly exposed to ionization continuum, $N_{\text{C}^{3+}}$ reaches the maximum at a much shorter distance along the line of sight from the illumination surface than $N_{\text{Al}^{2+}}$, N_{Mg^+} , N_{He^+} and $N_{\text{HI}^*(n=2)}$. This makes the CIV BAL easily saturated even when the BALs of Al III, Mg II, He I * and H α remain undetectable, as commonly shown in observations.

evidence for the long-sought inflows that directly feed the accretion disks and consequently the SMBHs. Our result demonstrates that the accretion disks in quasars are supplied with external gas transported inward from a distant inventory, at least in some objects.

Interestingly enough, the outer distance range of the inflow $3.2 \text{ pc} \simeq 3.3 \times 10^3 R_g$ is comparable to the radius of the postulated dusty torus, which was evaluated by the observed luminosity as the dust sublimation distance $R_{\text{sub}} \approx 3.0 \simeq 3.1 \times 10^3 R_g$ [23]. It is likely that the inflow headstreams set off from the dusty torus, a natural reservoir of gas supply within the sphere of influence of the SMBH. Part of the inflow gases may also originate from a highly extended disk suggested in some models[24] to connect the accretion disk and the torus, which is gravitationally unstable and clumpy. In both cases the inflow may be formed by gases drifting inward from all the azimuthal directions, resulting in an axially symmetric geometry for the bulk of the inflow. Several mechanisms may be responsible for removing the angular momentum of (a tiny) part of the gases therein, such as star-formation and stellar winds, collisions between clumps, tidal disruption of clumps by the SMBH[25–27]. The resulting gases with reduced angular momentum will spiral in via sub-Keplerian motion, among which those having the least angular momentum are accelerated to the fastest speeds as observed. The consideration of the residual angular momentum also favors an axial symmetric geometry for the bulk of the inflows. This raises an interesting postulate that the existence of a dusty torus in galactic nuclei, and the processes and efficiency to redistribute the specific angular momentum for gases therein, are essential for triggering, and determining the level of, quasar activity.

One important question to address is the ubiquity of the disk-feeding inflow in quasars. If the inflows are aligned at large inclination angles with respect to the axis of the general plane (e.g. in the case of originating from the torus; as shown in Figure 4), the vast majority of the LOS to the central radiation source that intersect the inflows are expected to be heavily obscured by the dusty torus. This makes the inflow essentially undetectable, except for those LOS passing at a grazing incidence angle to the upper surface of the torus, or passing through in-between clumpy clouds. The eight objects found with redshifted H_{n+2} and He I_n^* BALs out of 10^5 quasars may just be such extremely rare cases. This is supported by the fact that the optical-ultraviolet spectra of the eight objects are heavily reddened. Considering the difficulty in observation, the disk-feeding inflows as discovered here may actually be much more common in quasars than they appear to be, and should be considered as an indispensable component—the last piece of the puzzle that falls into place—for the paradigm of quasar black hole accretion.

Near the boundary of the inflow, gases with low (column) densities may disperse gradually, forming comet-like tails as spiraling in. If the tails get too dispersed to be shielded, they may be stopped and even reversed by the strong quasar radiation field, forming new (or becoming part of existing) shielding outflows. They may reveal themselves in blueshifted BALs of resonant metal ions, which can be more easily and commonly observed than redshifted H_{n+2} and He I_n^* BALs[9]. It is worth noting that both the location and physical conditions of the redshifted and blueshifted H_{n+2} and He I_n^* BALs are similar to those of the BELR in quasars. We found in our preliminary photoionization model calculations that the overall $H\alpha$ emission lines produced by the disk feeding inflow and the BAL outflow are comparable in strength to the BELs observed in quasars (Table 1

and Extended Data Fig. 11 in **Method**). It is tempting to hypothesize that the BELR is nothing special but merely a combination of the inflow, outflow, and accretion disk in quasars.

Acknowledgements This is a pre-print of an article published in Nature. The final authenticated version is available online at: <https://doi.org/10.1038/s41586-019-1510-y>.

The authors acknowledge the use of the Hale 200-inch Telescope at Palomar Observatory through the Telescope Access Program (TAP) that made these observations possible. Funding for SDSS-III has been provided by the Alfred P. Sloan Foundation, the Participating Institutions, the National Science Foundation, and the U.S. Department of Energy Office of Science. The SDSS-III Web site is <http://www.sdss3.org/>. H.Z., L.S. and X.P. acknowledge support by the National Natural Science Foundation of China (NSFC grant No. 11473025) and by the SOC program (CHINARE2017-02-03).

Author contributions H.Z. conceived the project. X.P. led the data acquisition and data reduction. X.S. analyzed the data and performed the photo-ionization simulations. W.Y., X.S., L.H., and G.L. contributed to writing the manuscript. All coauthors provided critical feedback to the text and helped shape the manuscript.

Author information The authors declare no competing financial interests. Correspondence and requests for materials should be addressed to H.Z. (zhouhongyan@pric.org.cn).

References

1. Schmidt, M. 1963. 3C 273 : A Star-Like Object with Large Red-Shift. *Nature* 197, 1040.
2. Netzer, H. 2013. *The Physics and Evolution of Active Galactic Nuclei. The Physics and Evolution of Active Galactic Nuclei*, by Hagai Netzer, Cambridge, UK: Cambridge University Press, 2013 .
3. Lynden-Bell, D. 1969. Galactic Nuclei as Collapsed Old Quasars. *Nature* 223, 690–694.
4. Krolik, J. H. 1999. Active galactic nuclei: from the central black hole to the galactic environment. *Active galactic nuclei: from the central black hole to the galactic environment*; /Julian H. Krolik. Princeton, N. J. : Princeton University Press, c1999.
5. Hu, C., Wang, J.-M., Ho, L. C., Chen, Y.-M., Zhang, H.-T., Bian, W.-H., Xue, S.-J. 2008. A Systematic Analysis of Fe II Emission in Quasars: Evidence for Inflow to the Central Black Hole. *The Astrophysical Journal* 687, 78–96.
6. Sulentic, J. W., Marziani, P., Zamfir, S., Meadows, Z. A. 2012. No Evidence for a Systematic Fe II Emission Line Redshift in Type 1 Active Galactic Nuclei. *The Astrophysical Journal* 752, L7.
7. Crenshaw, D. M., Kraemer, S. B., George, I. M. 2003. Mass Loss from the Nuclei of Active Galaxies. *Annual Review of Astronomy and Astrophysics* 41, 117–167.
8. Lu, H., Wang, T., Yuan, W., Dou, L., Ge, J., Zhou, H., Wang, H., Dong, X. 2008. Unsaturated Low-Ionization Broad Absorption Lines in the Quasar SDSS J144842.45+042403.1. *The Astrophysical Journal* 680, 858–866.
9. Hall, P. B., and 21 colleagues 2013. Broad absorption line quasars with redshifted troughs: high-velocity infall or rotationally dominated outflows?. *Monthly Notices of the Royal Astronomical Society* 434, 222–256.
10. Shi, X.-H., Jiang, P., Wang, H.-Y., Zhang, S.-H., Ji, T., Liu, W.-J., Zhou, H.-Y. 2016. The Redshifted Hydrogen Balmer and Metastable He I Absorption Line System in Mini-FeLoBAL Quasar SDSS J112526.12+002901.3: A Parsec-scale Accretion Inflow?. *The Astrophysical Journal* 829, 96.
11. Zhang, S., Zhou, H., Shi, X., Shu, X., Liu, W., Ji, T., Jiang, P., Sun, L., Zhou, J., Pan, X. 2015. Discovery of Extremely Broad Balmer Absorption Lines in SDSS J152350.42+391405.2. *The Astrophysical Journal* 815, 113.
12. Liu, W.-J., and 15 colleagues 2015. A Comprehensive Study of Broad Absorption Line Quasars. I. Prevalence of HeI* Absorption Line Multiplets in Low-ionization Objects. *The Astrophysical Journal Supplement Series* 217, 11.
13. Sun, L., and 12 colleagues 2017. Photoionization-driven Absorption-line Variability in Balmer Absorption Line Quasar LBQS 1206+1052. *The Astrophysical Journal* 838, 88.
14. Shi, X.-H., Pan, X., Zhang, S.-H., Sun, L.-M., Wang, J.-G., Ji, T., Yang, C.-W., Liu, B., Jiang, N., Zhou, H.-Y. 2017. Discovery of Variable Hydrogen Balmer Absorption Lines with Inverse Decrement in PG 1411+442. *The Astrophysical Journal* 843, L14.

15. Zhang, S., Zhou, H., Shi, X., Pan, X., Ji, T., Jiang, P. 2018. Ultra-dense Broad-line Region Scale Outflow in Highly Reddened Quasar SDSS J145057.28+530007.6. *The Astronomical Journal* 156, 4.
16. Hall, P. B. 2007. A Quasar with Broad Absorption in the Balmer Lines. *The Astronomical Journal* 133, 1271–1274.
17. Leighly, K. M., Dietrich, M., Barber, S. 2011. The Discovery of the First He I λ 10830 Broad Absorption Line Quasar. *The Astrophysical Journal* 728, 94.
18. Ji, T., and 13 colleagues 2015. Unshifted Metastable He I* Mini-broad Absorption Line System in the Narrow-line Type 1 Quasar SDSS J080248.18+551328.9. *The Astrophysical Journal* 800, 56.
19. Pâris, I., and 40 colleagues 2017. The Sloan Digital Sky Survey Quasar Catalog: Fourteenth Data Release. ArXiv e-prints arXiv:1712.05029.
20. Kaspi, S., Maoz, D., Netzer, H., Peterson, B. M., Vestergaard, M., Jannuzi, B. T. 2005. The Relationship between Luminosity and Broad-Line Region Size in Active Galactic Nuclei. *The Astrophysical Journal* 629, 61-71.
21. Greene, J. E., Ho, L. C. 2005. Estimating Black Hole Masses in Active Galaxies Using the H α Emission Line. *The Astrophysical Journal* 630, 122–129.
22. Cicone, C., and 14 colleagues 2014. Massive molecular outflows and evidence for AGN feedback from CO observations. *Astronomy and Astrophysics* 562, A21.
23. Netzer, H. 2015. Revisiting the Unified Model of Active Galactic Nuclei. *Annual Review of Astronomy and Astrophysics* 53, 365–408.
24. Collin, Z., Zahn, J. P. 1999. Star formation and evolution in accretion disks around massive black holes. *Astronomy and Astrophysics* 344, 433–449
25. Terlevich, R. 1996. Star-forming tori in Seyfert nuclei. *Vistas in Astronomy* 40, 17–22.
26. Wada, K., Norman, C. A. 2003. The Starburst-AGN Connection: Starburst-induced Obscuring Torus. *Active Galactic Nuclei: From Central Engine to Host Galaxy* 290, 261.
27. Wang, J.-M., Du, P., Brotherton, M. S., Hu, C., Songsheng, Y.-Y., Li, Y.-R., Shi, Y., Zhang, Z.-X. 2017. Tidally disrupted dusty clumps as the origin of broad emission lines in active galactic nuclei. *Nature Astronomy* 1, 775-783.
28. Drew, J. 1995. Emission Lines from Winds. *The Analysis of Emission Lines: A Meeting in Honor of the 70th Birthdays of D. E. Osterbrock & M. J. Seaton* 49.

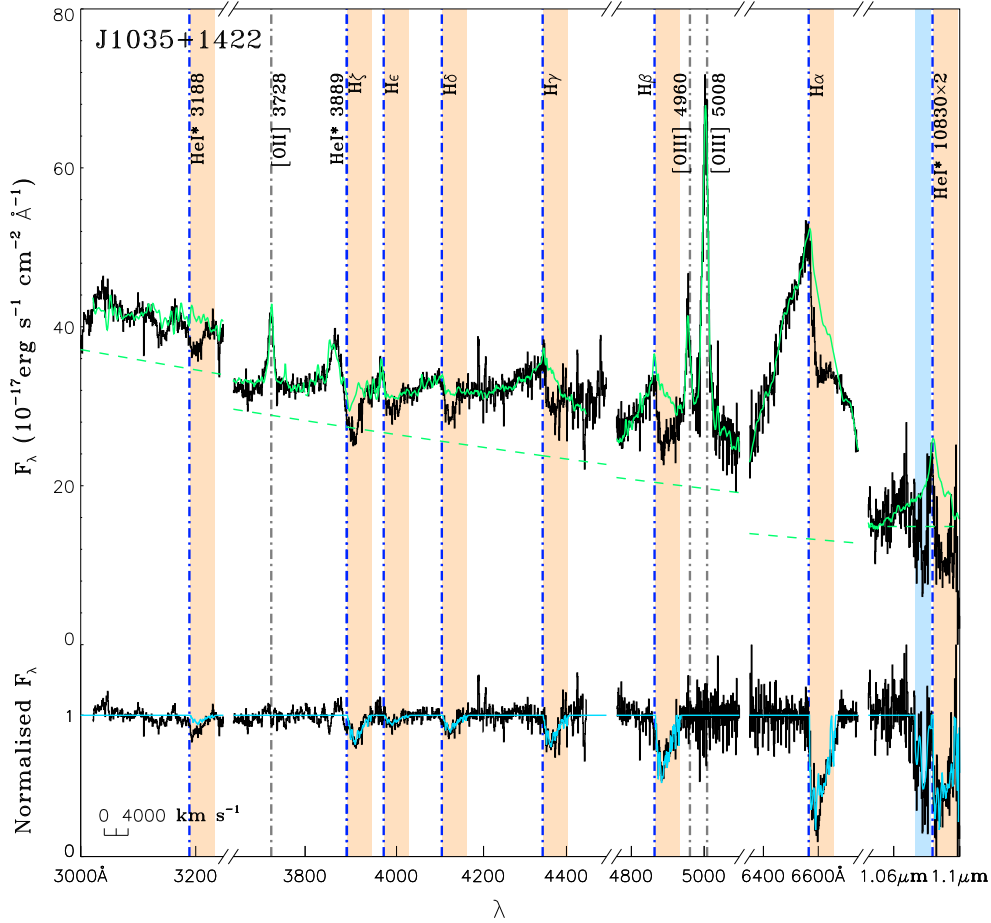


Fig. 1: Broad absorption lines (BALs) of the hydrogen Balmer series H_{n+2} and the meta-stable neutral helium multiplets HeI_n^* revealed in the rest-frame spectrum, from near-ultraviolet to near-infrared, of the quasar J1035+1422. In the upper part, the black line shows the observed flux, the green solid line represents the unabsorbed quasar template spectrum obtained by the ‘pair-matching’ method (see **Method**), and the green dashed lines show the underlying power-law continuum. In the lower part, the black line shows the normalized BAL spectrum. The redshifted BALs are normalized to the continuum only (with the modeled emission line flux subtracted), since they are found to be not obscuring the broad emission line region. The blueshifted $HeI^* \lambda 10830$ BAL is, in contrast, normalized using the total flux of the modeled template, as it is assumed to be fully obscuring both the continuum source and the broad emission line region. The cyan line represents the best-fit model BALs, which are employed to derive ion column densities from the H_{n+2} and HeI_n^* lines (The velocity profiles of the optical depth and covering factor for the $H\alpha$ BAL are shown in Extended Data Fig. 5 of **Method**). The blue dotted-dashed lines mark the rest wavelengths for the H_{n+2} and HeI_n^* transitions. The quasar systemic redshift is determined from narrow emission lines, including [OII] (marked as gray dotted-dashed vertical lines).

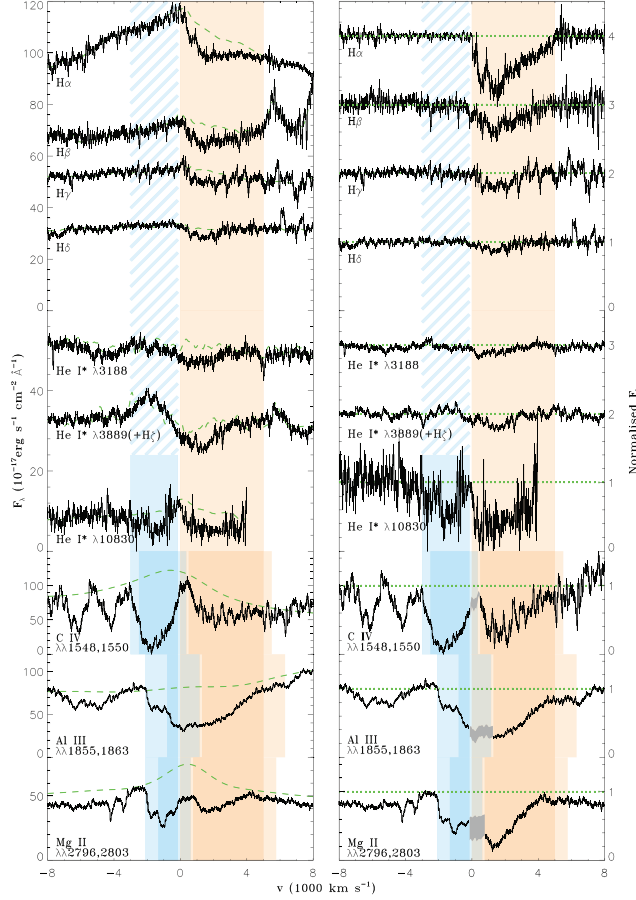


Fig. 2: Close-up of the observed (left) and normalized (right) BAL spectra of J1035+1422 in selected H Balmer ($H\alpha - H\delta$) and meta-stable He I* (He I* λ 10830, He I* λ 3889(+H ζ), and He I* λ 3189) in comparison with those of the metal lines, C IV, Al III, and Mg II, plotted in their common velocity space. The velocity ranges for the redshifted and blueshifted BAL systems (colored regions in red and blue respectively) are determined according to the normalized $H\alpha$ and He I* λ 10830 BAL spectra. The seeming velocity difference between H, He, and metal BALs are mostly due to the fact that all of the metal lines are actually doublets with a velocity offset of 500, 1,300, and 770 km s^{-1} between the member lines of C IV, Al III, and Mg II, respectively. The best-fit quasar composite spectrum is shown by the green dashed lines. It is obvious that the redshifted C IV trough is shallower than the blueshifted C IV trough and then the redshifted Mg II and $H\alpha$ troughs. The He I* λ 3889 line is severely blended with H ζ λ 3890, with a measured optical depth ratio of 0.7/0.3. Note that all of the H and He I* BALs show solely redshifted absorption troughs except for He I* λ 10830, the overwhelmingly strongest in strength of the multiplets. This implies drastically distinctive physical condition of the redshifted BAL gas from that of the blueshifted one. Unlike emission lines, which may be complicated by various effects, such as obscuration and projection, redshifted absorption lines are clean in kinematics and are of a robust indication for inward motion of the absorbing gas along the LOS[28].

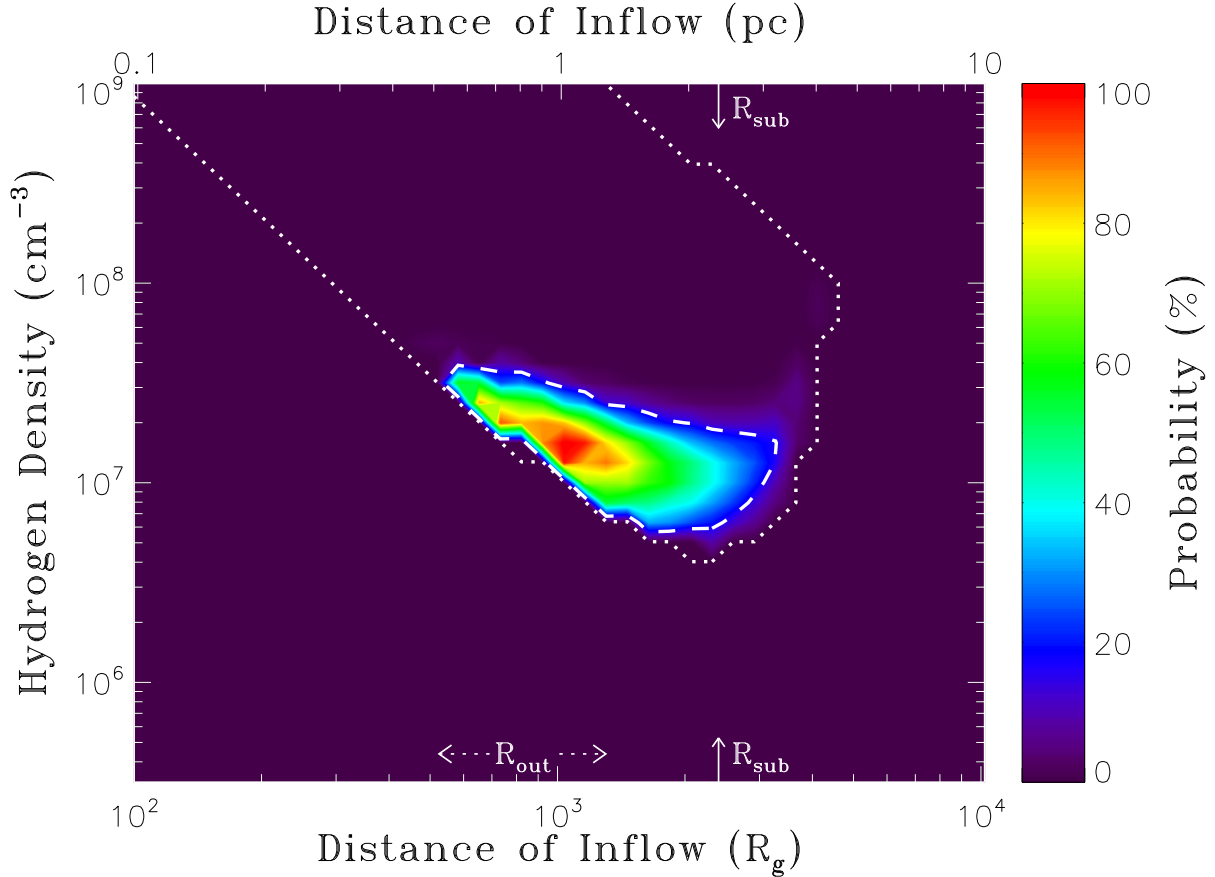


Fig. 3: Normalized probability density distribution in the parameter space of the total hydrogen density n_{H} and the characteristic distance R_{IF} of the inflow from the central black hole in J1035+1422. This is obtained by matching the photo-ionization models with the observed redshifted BALs of HI Balmer, He I*, C IV, and UV Fe II. The best-fit values are $n_{\text{H}} \approx 10^{6.75} - 10^{7.60} \text{ cm}^{-3}$ and $R_{\text{IF}} \approx 0.514 - 3.171 \text{ pc}$ (or $525 - 3,236 R_{\text{g}}$) at the 90% confidence level. Over-plotted are contours of the total hydrogen column density of the inflow models, indicating a well constrained range of $N_{\text{H}} \approx 10^{23.22} - 10^{23.79} \text{ cm}^{-2}$ (peaked at $N_{\text{H}} \approx 10^{23.46} \text{ cm}^{-2}$). The dotted arrows mark a postulated range of the outer accretion disk radius, which is taken as the previously reported disk radii derived from observations for a number of quasars with similar estimated self-gravity radii to that of J1035+1422, from $525 R_{\text{g}}$ (3C332) to $1,300 R_{\text{g}}$ (3C390.3). The dotted line shows the parameter envelope (90%) inferred by models without considering UV Fe II BALs. The inner surface of the dusty torus derived as the sublimation radius R_{sub} is indicated by the solid arrows for comparison. These results suggest that the inflow gas is dense and thick, and is located largely in between the accretion disk and the presumed dusty torus as sketched in Fig. 4.

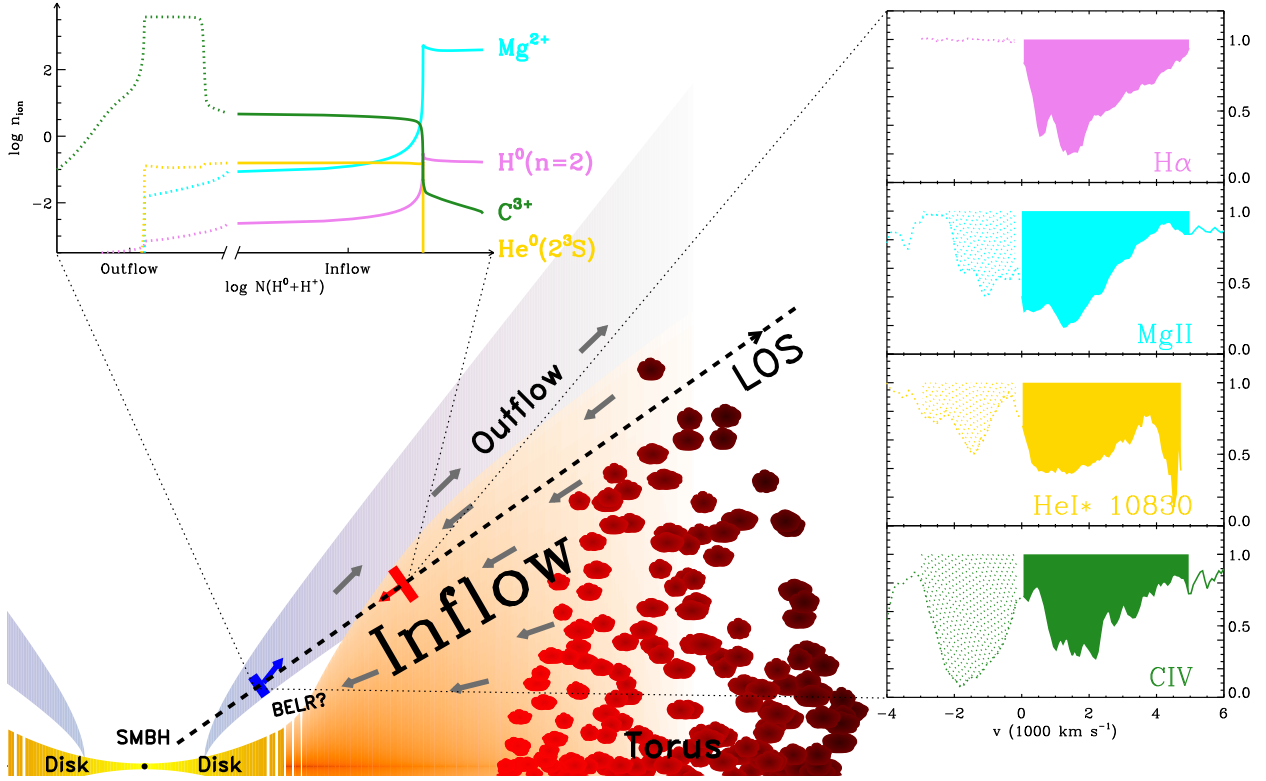


Fig. 4: Schematic view of the central engine of quasars with an inflow revealed by the hydrogen H_{n+2} and helium $He I_n^*$ BALs observed in J1035+1422 and its analogues. The inflow is positioned to be at parsec scale (about a thousand gravitational radii R_g of the black hole), located in-between an accretion disk and a dusty torus. The in-falling velocities of the gases along the line-of-sight (LOS) span from zero to as high as $5,000 \text{ km s}^{-1}$ (about the free-fall speed just beyond the outer radius of the accretion disk), indicating that the flow is being accelerated under the pull of the central SMBH. A large amount of cold, dense and high-column density gas as inferred from the BAL modeling provides direct and sufficient mass supply to feed the accretion disk. The inflow originates most likely from the torus, formed by materials therein that lose a substantial fraction of their angular momentum via various processes and hence fall inward. Viewed at a modest inclination angle, the LOS may intercept both the inflow and outflow, leaving imprints as both redshifted and blueshifted BALs that are observed in J1035+1422 (shown in the right inset are four representative BALs in their common velocity space). Color codes for the BALs: $H\alpha$ in magenta, Mg II in cyan, $He I^* \lambda 10830$ in yellow, and C IV in olive. The densities of the corresponding ions as a function of the depth along the LOS (represented by the total hydrogen column density $N_{H^0+H^+}$) are also shown in the upper-left inset with the same color code.

Methods

1 Diagnostic Sensitivity of the H I Balmer and He I* BALs within the Torus Scales.

The absorption lines in H I Balmer series and the meta-stable He I multiplets cover significantly wide ranges in both wavelengths and oscillator strengths. These advantages make them good probes to the physical properties of gaseous medium, much more powerful than the conventional resonant metal absorptions, such as C IV, Si IV or Mg II. We can measure the residual flux $f_r(\lambda)$ on an observed absorption-line spectrum. Assuming that the absorption-free flux is $f_0(\lambda)$, we have $f_r(\lambda) = f_0(\lambda) \cdot e^{-\tau(\lambda)}$, where $\tau(\lambda)$ is the optical depth determined by how much absorbing material there is along the LOS. The latter is often quantitatively described as the column density of the absorbing material. The optical depth at a given point in an absorption profile $\tau(\lambda)$ can often be well determined in a spectrum with good data quality when it is within the range of 0.05–3 (the corresponding normalized residual flux $e^{-\tau(\lambda)}$ is 0.95–0.05 in the absorption trough, meaning that the line is neither too weak nor severely saturated). Thus for H α at 6564 Å the measurable range of column density is $2.0 \times 10^{11} < \frac{dN_{\text{col}}(\text{H}_{n=2}^0)}{d\lambda} (\text{cm}^{-2} \text{Å}^{-1}) < 1.2 \times 10^{13}$, while for H κ at 3750 Å the measurable range is $1.9 \times 10^{14} < \frac{dN_{\text{col}}(\text{H}_{n=2}^0)}{d\lambda} (\text{cm}^{-2} \text{Å}^{-1}) < 1.1 \times 10^{16}$. Therefore, the Balmer series enables measurement of the column density over ~ 5 orders of magnitude. The He I* multiplets (e.g. He I* $\lambda 2829$ to He I* $\lambda 10830$) also covers a range of $8.9 \times 10^{10} < \frac{dN_{\text{col}}(\text{He}^0 2^3\text{S})}{d\lambda} (\text{cm}^{-2} \text{Å}^{-1}) < 6.8 \times 10^{15}$ or even wider. In contrast, the C IV $\lambda\lambda 1548, 1550$ doublet only covers a range of $1.2 \times 10^{13} < \frac{dN_{\text{col}}(\text{C}^{3+}_{\text{ground}})}{d\lambda} (\text{cm}^{-2} \text{Å}^{-1}) < 1.5 \times 10^{15}$.

In Extended Data Fig. 1 and Fig. 2, we show a simple demonstration of the diagnostic sensitivity of H I Balmer and He I* absorption lines. We assume that the central SMBH has a mass of $M_{\bullet} = 10^9 M_{\odot}$ and an Eddington ratio of 0.1. We place a slab of homogeneous absorbing gas with solar abundances at a distance d_{abs} to the central SMBH that varies from 10^2 to 10^4 gravitational radius R_g ($\equiv \frac{GM_{\bullet}}{c^2}$, i.e. roughly where the outflow is supposed to originate before reaching the dusty torus). The ionization (and the ionic column densities at the levels of interest) of the modeled gas is evaluated with the photo-ionization code CLOUDY (the latest version)[29]. Given $N_{\text{col}}(\text{H}_{n=2}^0)$ and $N_{\text{col}}(\text{He}^0 2^3\text{S})$ as functions of d_{abs} , the density n_{H} and total column density N_{H} of the gas, and assuming a Gaussian velocity dispersion corresponding to a full width at half maximum (FWHM) of 3,000 km s $^{-1}$, we can estimate the optical depths at line centers τ_{center} for various transitions. As long as τ_{center} is between 0.05 and 3, we consider the method sensitive for measuring the corresponding ionic column densities.

The colored area in the plots shows the sensitive range for each individual line. For $N_{\text{H}} = 10^{20} \text{ cm}^{-2}$, only denser and farther-away medium has enough neutral gas to render considerable optical depths in H α and He I* $\lambda 10830$ lines. When N_{H} increases, $N_{\text{col}}(\text{H}_{n=2}^0)$ and $N_{\text{col}}(\text{He}^0 2^3\text{S})$ also increase. At a certain point, these ionic column densities are so large in gas with intermediate density that H α and He I* $\lambda 10830$ become saturated. While higher-order lines with smaller oscillator strengths (e.g. H δ and He I* $\lambda 3889$) become sensitive probes, instead. Therefore, by

including the whole series of H I Balmer and He I* lines, we can reliably measure $N_{\text{col}}(\text{H}_{n=2}^0)$ and $N_{\text{col}}(\text{He}^0 2^3\text{S})$ in the vast majority of the parameter space of our interest, especially for thick medium ($N_{\text{H}} > 10^{22} \text{ cm}^{-2}$).

2 Redshifted H I Balmer/He I* BAL and Mini-BAL Systems in Quasars.

Through a systematic search for H I Balmer and He I* absorption systems in the SDSS quasar catalog ($\sim 10^5$ quasars with $z < 1.3$), we find ~ 50 such systems with He I* $\lambda 3889$ absorption and at least three Balmer absorption lines detected at $> 3\sigma$ significance. NAL, mini-BAL, and BAL systems account for $\sim 1/3$ of this sample, respectively. $\sim 1/2$ show net blueshifted troughs, $\sim 1/4$ show net redshifted troughs, while in the rest $\sim 1/4$ the troughs are either unshifted or extend both bluewards and redwards. Of great interest are those systems with redshifted BAL or mini-BAL troughs, which are candidates of inflows proximate to their central engines. In Extended Data Fig. 3, we present seven additional objects manifesting redshifted BALs or mini-BALs for H I Balmer and He I* absorptions, besides J1035+1422. One of the mini-BAL systems, the H I Balmer and He I* absorption system in J1125+0029, has been scrutinized and confirmed to be a parsec-scale inflow[10], even though we could not confirm if the inflow can go further into the center to directly feed the accretion disk around the the central SMBH. This is because that the H I Balmer and He I* absorption only trace the intermediate- to low-ionization and neutral regions in the absorbing medium. Since the SDSS spectra of these objects cover wavelengths no shorter than $1,700 \text{ \AA}$ in their rest frame, the high-ionization lines (C IV, Si IV, and N V doublets, etc.) are all missed out. Hence, we know little about the highly ionized region in the absorbing medium, and the potential relation between the redshifted Balmer/He I* BAL or mini-BAL systems and the most common HiBAL (high-ionization BAL) systems (whether redshifted or blueshifted).

J1035+1422 is also listed in our catalog of redshifted H I Balmer/He I* BAL quasars, showing the largest width of absorption troughs therein. The multiple archival and our follow-up spectroscopic observations have ensured the wavelength coverage from C IV $\lambda\lambda 1548, 1550$ to He I* $\lambda 10830$. Therefore, both high- and low-ionization lines can be measured, and the absorbing gas along the line of sight could thus be explored further. In the following sections, we present a detailed analysis on the BAL systems in J1035+1422 and characterize their roles in the theoretical scheme of the quasar structure.

3 Optical and NIR Spectroscopic Observations, and Data Reduction.

The BOSS spectrum for J1035+1422 was observed on March 24, 2012 with an exposure time of 4,500 s. We conducted a follow-up campaign aiming at this object with the intermediate-resolution DoubleSpec and TripleSpec spectrograph equipped on the Palomar 200-inch Hale telescope in the optical and NIR. The DoubleSpec data were obtained on Apr 23, 2014 with a total exposure of 4×500 s, and the TripleSpec data were acquired on Mar 13, 2017 with a total exposure of 12×120 s. An archival broad-band optical-to-NIR spectrum is also available, which was obtained by VLT/X-shooter on Dec 6, 2014 through the ESO program 094.A-0087(A), with a spectral resolution of

$R \equiv \lambda/\Delta\lambda \sim 10,000$. The total exposure time is ~ 40 min. We follow the standard procedure in reducing the raw data, using IRAF² and the IDL SpexTool package[30]. The Catalina³ monitoring of J1035+1422 shows negligible variability in V-band during a period of 8 years (2005 Apr 9 to 2013 Oct 26). Thus, We combine the relatively low resolution BOSS and DoubleSpec/TripleSpec data and use the combined spectrum to calibrate the X-shooter échelle spectrum. The BAL troughs are clearly resolved in the X-shooter spectrum.

4 The Central Engine.

Though the rest-frame UV through optical to NIR color of J1035+1422 is the bluest in the sample of quasars with redshifted H I Balmer and He I* absorption lines, it is obviously redder than normal optically-selected quasars. Using the SDSS quasar composite spectrum[31] reddened with the SMC-type extinction curve[32] to match the flux in the absorption-free windows in the rest-frame UV band, we find $E(B - V) \approx 0.12$, implying a significant amount of dust reddening.

We estimate the mass of the central SMBH using the $H\alpha$ broad emission line width and the rest-frame optical luminosity, and adopting the radius-luminosity scaling relation[21]. The monochromatic luminosity at 5100 Å in the quasar’s rest-frame, L_{5100} , is derived using the measured $f_\lambda(5100 \text{ Å})$ and assuming a cosmology with $H_0 = 70 \text{ km s}^{-1} \text{ Mpc}^{-1}$, $\Omega_M = 0.3$ and $\Omega_\Lambda = 0.7$. Compared to Mg II and $H\beta$ emission lines, the $H\alpha$ peak is less affected by the absorption trough. Therefore, we use the width of the broad $H\alpha$ emission line (FWHM $\approx 1.4 \times 10^4 \text{ km s}^{-1}$) to estimate the black hole mass, and yield $M_{\text{BH}} \approx 2.0 \times 10^{10} M_\odot$. Adopting a bolometric luminosity of $L_{\text{bol}} = (8.1 \pm 0.4) L_{5100}$ [37] and assuming an accretion efficiency of 0.1, we estimate the mass accretion rate to be $\dot{M}_\bullet \approx 13 M_\odot \text{ yr}^{-1}$.

The sizes of quasar accretion disks are difficult to determine, and they are generally thought to be of the order from several hundred to a few thousand gravitational radii. Theoretical models assume the self-gravity radius $R_{\text{sg}} \simeq 6.04 \times 10^4 \alpha^{2/9} \eta^{-4/9} M_\bullet^{-2/9} (L_{\text{bol}}/L_{\text{Edd}})^{4/9}$ to be a natural outer disk boundary, where the vertical component of the central gravity is balanced by the self-gravity of the disk, and $\alpha \sim 0.01 - 1$ is the viscosity parameter and $\eta \equiv L_{\text{bol}}/\dot{M}_\bullet c^2 \sim 5.7 - 42\%$ the accretion efficiency[23]. Beyond this boundary the disk becomes gravitationally unstable and starts to fragment into clumps, forming gaps that prevent efficient mass accretion. We estimated a self-gravity radius $R_{\text{sg}} \approx 140 R_g$ in J1035+1422 for $\alpha = 0.3$ and $\eta = 10\%$. Observationally, R_{out} can be well modeled in a few percent of quasars with double-peaked emission line profiles. For some of those with the estimated self-gravity radii similar to that of J1035+1422 within a factor of two (namely 3C 332, Pictor A, 3C 17, Arp 102B, and 3C 390.3), their modeled outer disk radii as available from the literature [33–36] fall into $R_{\text{out}} \sim 540 - 1,300 R_g$. We thus consider the outer disk radius of J1035+1422 to lie somewhere from a few hundred to about one thousand gravitational radii.

²<http://iraf.noao.edu/>

³<http://nesssi.cacr.caltech.edu/DataRelease/>

5 The BAL Systems.

The redshifted BAL troughs can be easily identified for various transitions, including the H I Balmer series, the meta-stable He I* $\lambda\lambda$ 3,188, 3,889, 10,830, C IV $\lambda\lambda$ 1,548, 1,550, Al III $\lambda\lambda$ 1,854, 1,862, and Mg II $\lambda\lambda$ 2,796, 2,803. For He I* λ 10830, C IV, and Mg II, separate, blueshifted troughs are also clearly observed, while for Al III doublets with a larger wavelength interval between its two transitions, the blueshifted BAL trough only extends bluewards smoothly. For Balmer lines and other weaker He I* lines, no evident blueshifted BAL absorption has been detected. Furthermore, comparing the spectra with the SDSS quasar composite, we find that considerable rest-frame UV flux is absorbed by Fe II between rest-frame 2,000 and 2,800 Å, and wavelengths straddling rest-frame 1,600 Å. Due to the numerous line transitions at these wavelengths, the absorption troughs overlap seriously with each other, rendering it impossible to identify the profile of any individual BALs.

6 Measurement of the Redshifted BALs.

The redshifted H I Balmer BALs, from H α to H ϵ can be readily identified on the observed spectrum of J1035+1422 with absorbing troughs within the velocity range from ~ 0 to $\sim 5,000$ km s $^{-1}$ with respect to the quasar's rest-frame accurately determined by narrow emission-lines, including [O II] λ 3727 and [O III] $\lambda\lambda$ 4959,5007. Due to its relative weakness (λf_{ij} ratio of 2.42 between H ϵ \equiv H $_7$ and H η \equiv H $_9$), redshifted H η BAL is only marginally detected with a similar velocity structure. H ζ \equiv H $_8$ λ 3890 should also be present, but it is heavily blended with He I* λ 3889. We use the pair-matching method to recover the absorption-free spectrum[12, 38] of J1035+1422. The underlying assumption is that if the spectrum of a non-BAL quasar resembles the spectrum of a given BAL quasar in the absorption-free portions, they are intrinsically similar, and the non-BAL quasar then provides a good approximation to the unabsorbed flux striding over the BAL troughs. We choose non-BAL quasars from the BOSS quasar catalog, and fit the spectra with that of J1035+1422. The wavelength ranges affected by BAL troughs ($v \sim 0 - 5,000$ km s $^{-1}$ for the above mentioned Balmer lines) are masked out during the fit. If the reduced $\chi^2 < 1.5$, we consider it an acceptable match. The mean spectrum of all accepted non-BAL quasar spectra is used as the unabsorbed template, and the variance is used to estimate the uncertainty of the template.

From the spectra normalized using the template, we can derive the covering factor and the optical depth for the redshifted Balmer BALs as a function of velocity shift v following

$$\begin{aligned} I_{H\alpha}(v) &= [1 - C_f(v)] + C_f(v)e^{-\tau_{H\alpha}(v)} \\ I_{H_i}(v) &= [1 - C_f(v)] + C_f(v)e^{-\tau_{H\alpha}(v)\lambda_{H_i}f_{H_i}/\lambda_{H\alpha}f_{H\alpha}} \end{aligned} \quad (1)$$

where $I(v)$ is the normalized flux, $C_f(v)$ is the covering factor, and $\tau(v)$ is the optical depth.

In practice, because of the relatively broad widths of the BAL troughs and the diversity of the

profiles that the emission lines may have, the pair-matching and the profile extraction are performed iteratively: an initial guess for the red wings of the emission peaks is used as a rough estimate for the BAL profiles. Based on the absorption corrected spectra derived by employing these profiles, a more realistic template can be further achieved. This procedure continues until a set of self-consistent emission template and absorption profiles are finally obtained.

The resultant template for H I Balmer emissions is plotted in Figure 1 in the main text. Even if based on a premature template, we can see that the depth of the apparently unsaturated H α trough is not significantly larger than H β . This is hard to explain considering the large λf_{ij} ratio of 7.26 between H α and H β , unless we assume the absorbing medium only obscures part of the background continuum source, leaving the emission line region unobscured. In this analysis, we adopt this assumption so that the normalized flux used in Eq.1 is evaluated by removing the emission lines of the template and dividing the residual spectrum by the continuum. The resultant covering factor and true optical depth as a function of velocity shift, are plotted in Extended Data Fig. 5.

The integral $\int \tau_{\text{H}\alpha}(v) dv$ through the BAL trough yields a column density of $N_{\text{col}}(\text{H}_{n=2}^0) = 1.98 \pm 0.14 \times 10^{15} \text{ cm}^{-2}$ for the redshifted system. The column density at the meta-stable He 0 level 2 3 S of the same absorbing gas is measured using He I* $\lambda 3889$, given that the He I* multiplets and the Balmer series BAL are found to share the same absorption profile. (In fact, we find the normalized spectrum of redshifted He I* $\lambda 10830$ BAL, which is deemed fully saturated, can be well described by the profile of the covering factor $C_f(v)$ derived from Balmer BALs, see Fig. 2.) By removing the contribution of H δ absorption from the trough at rest-frame $\sim 3,900 \text{ \AA}$ and applying the fractional distribution $\tau(v) / \int \tau(v) dv$ extracted from Balmer series, we find $N_{\text{col}}(\text{He}^0 2^3\text{S}) = 1.11 \pm 0.14 \times 10^{15} \text{ cm}^{-2}$.

The absorption troughs of metal lines in the range of $\sim 1,500 - 3,300 \text{ \AA}$ relative to the quasar's rest-frame, including C IV, Al III, Fe II, Mg II, etc., are hard to characterized. Both the UV Fe II and the redshifted BAL doublets of those alkaline-like metal ions show seriously overlapping troughs. And with blueshifted absorptions present for at least C IV, Al III, and Mg II, the absorption-free windows in the rest-frame UV band is too limited to reveal the unabsorbed flux through the pair-matching method. The initial fitting using SDSS quasar composite suggests that the spectra around rest-frame 1,500, 1,600, 1,960, 1,980 and 3,100 \AA are minimally affected by absorption, consistent with our knowledge on the wavelength distribution of Fe II multiplets.

7 Photo-ionization Models of the Reshifted BAL Inflow

The primordial model Since all gaseous medium is in the vicinity of the central SMBH, the ionization state of the inflowing gas giving rise to the redshifted absorption system is dominated by the radiation from the central engine. To estimate the physical conditions, we employ CLOUDY to simulate the physical processes in the medium. The simplest model is a slab of gas with a uniform density and chemical composition, irradiated directly by the central continuum source. Such primordial models can be fully described using parameters including n_{H} , N_{H} , ionization parameter at the inner (illuminated) surface U , abundance of elements, and the spectral energy

distribution (SED) of the incident radiation. The CLOUDY models use these parameters and output the column densities of various ions observed in absorption lines. Comparing the output with our measurements, we can assess which values of the model parameters are reasonable.

A typical AGN continuum is employed as the incident SED, which is a combination of a UV bump described as $\nu^{\alpha_{UV}} \exp(-h\nu/kT_{BB}) \exp(-kT_{IR}/h\nu)$ and power law $a\nu^{\alpha_X}$. The UV bump is parameterized by a UV power-law index of $\alpha_{UV} = -0.5$, and an exponentially cut-off with a temperature $T_{BB} = 1.5 \times 10^5$ K at high energy and $kT_{IR} = 0.01R_{yd}$ in the infrared. The power-law component has an index $\alpha_X = -2$ beyond 100 keV, and -1 between 1.36 eV and 100 keV. The overall flux ratio of X-ray to optical is $\alpha_{OX} = -1.4$.

For the absorption gas with given n_H and U , the model can give a specific value of N_H with which the predicted $N_{col}(H_{n=2}^0)$ and $N_{col}(He^0 2^3S)$ best match the measurements. The differences between the predicted values by this optimal N_H and the measurements allow us to evaluate a ‘probability density’: $P \propto \prod_i e^{-\frac{1}{2} \left(\frac{N_{col}^{theo}(ion_i) - N_{col}^{meas}(ion_i)}{\sigma(N_{col}^{meas}(ion_i))} \right)^2}$, where i stands for different ions. If even for the optimal N_H the differences are far beyond the measurement uncertainties, the given n_H and U appear rather impossible. In Extended Data Fig. 6 panel (a), we plot the distribution of this ‘probability density’ as a function of density n_H and distance d_{inflow} (in units of R_g) from the central SMBH. The distance d_{inflow} is derived as $\frac{L(\lambda < 912)}{4\pi d_{inflow}^2} = U n_H c \overline{E_{ph}(\lambda < 912)}$, where $L(\lambda < 912)$ is the ionizing luminosity of the continuum source and $\overline{E_{ph}(\lambda < 912)}$ is the average energy for all ionizing photons. The zone with high probability density is a narrow, curved belt with d_{inflow} between 35 and 4,000 R_g and n_H between 10^8 and $10^{10.5} \text{ cm}^{-3}$.

These highly probable models predict very large column densities for high-ionization ions, e.g., $N_{col}(C_{ground}^{3+}) > 4 \times 10^{17} \text{ cm}^{-2}$, and thus we would expect $\tau_{C\ IV}(v) \gg 1$ throughout the redshifted BAL trough. However, these predictions do not seem to agree with the observation. Though the metal lines cannot be measured as straightforwardly as either the H I Balmer or the He I* lines, an alternative strategy can be employed to evaluate whether the predicted values are consistent with the observation. Considering that C IV absorption has the same $\tau(v)$ and $C_f(v)$ profile as that of He I*, we present in Extended Data Fig. 7 the model spectra, where the flux absorbed by C IV is recovered for $\log N_{col}(C_{ground}^{3+})(\text{cm}^{-2}) = 15, 16$ and 17 . When the column density well exceeds 10^{16} cm^{-2} , in which case $\tau_{C\ IV}(v) > 1$ throughout the redshifted BAL trough, the recovered C IV emission line peak seems to behave abnormally, in contrast to the smooth appearance and the consistence with the best-fit composite if the column density is about 10^{16} cm^{-2} . Accordingly, we believe that the most possible value for $\log N_{col}(C_{ground}^{3+})(\text{cm}^{-2})$ is around 15.8 with uncertainty of about 1.1, significantly smaller than the prediction. (Even for very metal-poor gas of $0.1 Z_{\odot}$, primordial simulation models predict $N_{col}(C_{ground}^{3+}) > 10^{17} \text{ cm}^{-2}$.)

Post C^{3+} region models Detailed investigations on the ionization structure of the primordial models reveal that C^{3+} ions, which are created by ionizing photons with $h\nu > 47.9$ eV, tend to arise in the region in front of the H I region. Beyond the C^{3+} region, with high energy photons exhausted, high-ionization ions (e.g. C^{3+} , Si^{3+} , etc.) are negligible and low-ionization ions and neutral atoms

(e.g. Mg^+ , H^0) become dominant (see Extended Data Fig. 9 panel (a)). it is therefore more reasonable to use the region lying behind the C^{3+} region (the ‘post- C^{3+} region’ for short) in the primordial models to estimate the physical conditions and environment of the observed inflow, rather than using the entire primordial models.

Still employing the primordial setup for photo-ionization simulations, for a gaseous slab with given n_{H} and U , now we try to find if there is a pair of N_{H} values for gas between which the simulation predicts $N_{\text{col}}(\text{H}_{n=2}^0)$, $N_{\text{col}}(\text{He}^0 2^3\text{S})$, and $N_{\text{col}}(\text{C}_{\text{ground}}^{3+})$ within the uncertainty of our measurements. If such N_{H} values are found, they mark the inner and outer surfaces of the model suitable for the inflow. One sample is illustrated in Extended Data Fig. 9 panel (a) for a primordial model with $n_{\text{H}} = 10^7 \text{ cm}^{-3}$ and $U = 10^{0.5}$ ($d_{\text{inflow}} \approx 1,500 R_{\text{g}}$). The suggested inner surface of the inflow model coincides with the furthest extension of the C^{3+} region. ‘Probability density’ is estimated in the same way with $N_{\text{col}}(\text{C}_{\text{ground}}^{3+})$ included. As shown in Extended Data Fig. 6 panel (b), the zone corresponding to high ‘probability density’ moves downwards, with smaller n_{H} between 10^7 and 10^{10} cm^{-3} . The ‘probability density’ now presents a bimodal distribution peaked at $n_{\text{H}} \approx 10^7 \text{ cm}^{-3}$ and $d_{\text{inflow}} \approx 2,000 R_{\text{g}}$, and $n_{\text{H}} \approx 10^{9.5} \text{ cm}^{-3}$ and $d_{\text{inflow}} \approx 100 R_{\text{g}}$, respectively.

Further constraints can be introduced using another prominent absorption feature, the UV Fe II multiplets. The Fe^+ ion presents the largest number of levels in all metal ions abundant in astrophysical gaseous medium. Following the strategy of recovering absorbed flux according to the simulations’ prediction as for C IV, UV Fe II can reveal more information about the absorbing medium than Mg II and Al III doublets, which originate from single levels and the lines are saturated in our case. The result strongly favors a ‘probability density’ peak around $n_{\text{H}} \approx 10^7 \text{ cm}^{-3}$. In Extended Data Fig. 8, we plot the recovered flux of UV Fe II bump between rest-frame 2,000 and 2,700 Å, using the models of high probability shown in Extended Data Fig. 6 panel (b) ($\log n_{\text{H}}(\text{cm}^{-3}) = 7, 7.5, 9$ and 9.5 , respectively). The lowest 371 levels of Fe^+ and the lowest 15 levels of Cr^+ and Ni^+ are considered. While the $n_{\text{H}} = 10^{9.5} \text{ cm}^{-3}$ model suggests no contribution from UV Fe II absorption at all, the $n_{\text{H}} = 10^7 \text{ cm}^{-3}$ model predicts saturated absorptions for not only transitions of UV 1,2,3 multiplets at around 2,300 and 2,600 Å from the ground term, but also transitions from/between excited levels. The best-fit composite (blue dashed curve in Extended Data Fig. 8) is consistent with the models with $\log n_{\text{H}}(\text{cm}^{-3}) \sim 7 - 7.5$. Therefore, considering the Fe II absorption, we can definitely rule out the models around the upper-left ‘probability density’ peak at $\log n_{\text{H}}(\text{cm}^{-3}) = 9.5$ in Extended Data Fig. 6 panel (b). The distribution of the updated ‘probability density’ $P' = P \times P_{\text{UV Fe II}}$ is plotted in Figure 3 in the main text, where $P_{\text{UV Fe II}}$ is estimated using the χ^2 of the model corrected for UV Fe II bump. The models of high ‘probability density’ is now restricted to a small area around $\log n_{\text{H}}(\text{cm}^{-3}) \approx 7.1$ and $d_{\text{inflow}} \approx 1,100 R_{\text{g}}$.

Radiative pressure on the inflow The radiative pressure of an electromagnetic wave is $P_{\text{rad}} = \frac{I_f}{c}$, where I_f is the energy flux. Therefore, given a radiation field at the inner and outer surfaces of the modeled inflow, we can estimate the radial force on the inflow due to the radiative pressure. $\frac{F_{\text{rad}}}{s_{\text{inflow}}} = P_{\text{rad,incid}} + P_{\text{rad,reflc}} - P_{\text{rad,trans}} - P_{\text{rad,diff}}$, where $P_{\text{rad,incid}}$, $P_{\text{rad,reflc}}$, $P_{\text{rad,trans}}$, $P_{\text{rad,diff}}$ are pressures of incident, reflected, transmitted, and outwards diffuse emitting radiation, and s_{inflow} is

the irradiated area of inflow. For the best inflow model, the outward radiative force amounts to only $\sim 1.2 - 1.9\%$ of the gravitational force, where the uncertainty mostly comes from different assumptions of the angular distribution of reflected and diffuse emitting radiation.

If the gravitational force and the radiative resistance are the only forces exerted on the inflow, the motion will be approximately free-fall. According to the current estimated distance and kinetic energy of the inflow, we find that the radial velocity equals zero at a distance of about 1.5 pc or $\approx 1,500 R_g$. This is similar to the dust sublimation radius $R_{\text{sub}} \approx 2,000 R_g$ estimated using the observed luminosity[39] of J1035+1422, suggesting the inner surface of the dusty torus as a natural embarkation point of the inflow.

Mass flux rate of the inflow The simplest picture of the inflow detected in redshifted BALs is discrete clouds. In this picture, the mass inflow rate can be estimated as $\dot{M}_{\text{inflow}} = \mu m_p N_{\text{H,inflow}} f_f 4\pi d_{\text{inflow}}^2 \Omega_{\text{inflow}} / t_{\text{in}}$, where $\mu \approx 1.4$ is the mean atomic mass per proton, m_p is the mass of a proton, f_f is the local filling factor, Ω_{inflow} is the unknown global covering factor of the inflow structure, and t_{in} is the in-falling time scale, i.e. $d_{\text{inflow}}/v_{\text{in}}$. Using the optical depth $\tau(v)$ -weighted mean of $C_f(v)$ and v in Eq.1 as f_f and v_{in} , respectively, we have $\dot{M}_{\text{inflow}} \approx 61 \Omega_{\text{inflow}} M_{\odot} \text{ yr}^{-1}$, where Ω_{inflow} is roughly equal to Ω_{torus} at ~ 0.6 under the assumption that the inflow originates from the inner surface of the dusty torus.

An alternative picture is that the inflow structure is a continuous layer that our LOS intercepts with an angle of i_{in} . The observed red-shift velocity is $v_{\text{in,obs}} = v_{\text{in}} \cos i_{\text{in}}$. The mass inflow rate is estimated by calculating the amount of gas passing through a given cross section at d_{inflow} in the layer in unit time:

$$\begin{aligned} \dot{M}_{\text{inflow}} &= \mu m_p 2\pi d_{\text{inflow}} \int_h n_{\text{H}} f_f(h) v_{\text{in}}(h) dh \\ &= \mu m_p 2\pi d_{\text{inflow}} \int_l n_{\text{H}} f_f(l) v_{\text{in,obs}} / \cos i_{\text{in}} dl \sin i_{\text{in}} \\ &= \mu m_p 2\pi d_{\text{inflow}} \int_{v_0}^{v_1} dN_{\text{H}} / dv_{\text{in,obs}} C_f(v_{\text{in,obs}}) v_{\text{in,obs}} dv_{\text{in,obs}} \tan i_{\text{in}} \end{aligned} \quad (2)$$

where h is the height of the inflow layer at a distance d_{inflow} , l is the length along the LOS, and v_0 and v_1 are the observed minimum and maximum radial velocities in the redshifted trough, respectively. The result is $\dot{M}_{\text{inflow}} \approx 30 \tan i_{\text{in}} M_{\odot} \text{ yr}^{-1}$. However, since only the medium in the LoS is detected, the entire structure of the inflow and its configuration relative to the accretion disk and torus remains to be explored.

8 Blueshifted BAL Outflow as a Shielding Medium

SED-constrained blueshifted BAL outflow model Using the post-C³⁺ region in primordial photo-ionization models to explain the physical conditions of inflow in J1035+1422, we suggest that the radiation illuminating the inflow is very different from the original radiation from the cen-

tral engine. In Extended Data Fig. 9 panel (c), we show the transmitted SED passing through the C^{3+} region for the primordial model with $\log U = 0.5$ and $\log n_H(\text{cm}^{-3}) = 7$. The most prominent difference is the absence of photons with $h\nu > 48 \text{ eV}$ ($\lambda < 260 \text{ \AA}$). This SED may be a good approximation to the actual incident radiation illuminating the inner surface of the inflow.

The difference between the typical quasar SED and the SED required by the inflow model is so significant that we have to postulate that there is some kind of shielding gas obscuring the central engine, as seen from the inflow (this is preferred over an alternative assumption that the central engine of our object is intrinsically abnormal). In the aspect of absorbing high energy photons, the shielding gas is equivalent to the C^{3+} and pre- C^{3+} regions (the region in front of C^{3+} region where even higher-ionization ions dominate) in the primordial models.

The blueshifted BALs consisting of C IV, Al III, Mg II doublets and He I* $\lambda 10830$ tracing a massive outflow presents a good candidate for the shielding gas. The absence of H I Balmer absorptions in the blueshifted BAL system implies that the outflow is more highly ionized than the BAL inflow, and thus is probably closer to the central engine than the latter. In addition, the residual flux under the blueshifted C IV BAL trough approach zero at the deepest point, indicating that the absorber fully cover at least the inner part of the continuum source along the LOS. Therefore, as seen from the inflow, the object appears to be a blueshifted LoBAL quasar.

BAL quasars are known to be weak in the soft X-ray band[40] due to strong absorption[41]. The X-ray flux of our inflow-illuminating radiation is also expected to be heavily depressed. The quantity $\Delta\alpha_{\text{OX}} = \alpha_{\text{OX}}(\text{observed}) - \alpha_{\text{OX}}$ was often used to characterize the X-ray weakness of the BAL quasars in their sample compared with non-BAL quasars, where $\alpha_{\text{OX}}(\text{observed})$ is the logarithm of the ratio between the observed monochromatic luminosities L_ν at 2 keV and 2500 \AA , and α_{OX} is the same quantity for a typical non-BAL quasar[42]. The X-ray depression is found to be more severe in LoBAL quasars than in HiBAL quasars, because the sub-sample of LoBAL quasars has systematically smaller $\Delta\alpha_{\text{OX}}$.

The predicted flux depression at 2 keV is plotted in Extended Data Fig. 9 panel (c), where the average values of $\Delta\alpha_{\text{OX}}$ for HiBAL and LoBAL samples has been assumed, respectively. The anticipated inflow-illuminating flux is even lower than the average value for LoBAL sample. However, due to the fact that the majority of BAL quasars remain undetected in X-ray as yet, these ‘average’ values are likely to be some kind of upper limits.

Further quantitative analysis suggests that, for the post- C^{3+} inflow model, the transmitted SED of any gaseous plate with the same U and N_H as the pre- C^{3+} and C^{3+} regions associated with the post- C^{3+} inflow can match the incident SED required by the inflow. For example, in Extended Data Fig. 9 panel (b) we present the shielding gas model with $\log U = 0.5$, $\log n_H(\text{cm}^{-3}) = 9.5$, and $\log N_H(\text{cm}^{-2}) = 23.5$, through which the transmitted SED matches the incident SED required by the inflow model with $\log n_H(\text{cm}^{-3}) = 7$ shown in Extended Data Fig. 9 panel (a), noticing that for the associated pre- C^{3+} and C^{3+} regions $\log U = 0.5$ and $\log N_H(\text{cm}^{-2}) = 23.56$. Since U is fixed, the denser the shielding gas is, the closer it is to the central engine. In the given example,

as n_{H} for the shielding gas model is 2.5 orders of magnitude larger than the inflow model, the corresponding outflow is inferred to be much closer to the central engine, at $\sim 82 R_{\text{g}}$.

Comparison with the observation of blueshifted BAL system However, these models seem inconsistent with the measurements for the blueshifted BAL systems. Since the blueshifted C IV BAL trough is saturated, we can only derive rather loose constraints that $N_{\text{col}}(\text{C}_{\text{ground}}^{3+})$ should not be smaller than a few 10^{15} cm^{-2} . If we assume that the outflow fully obscures the continuum source and the emission region as the C IV trough indicates, we find that the blueshifted He I* $\lambda 10830$ are unsaturated, making the measurements of $\tau(\nu)(\text{HeI}*\lambda 10830)$ feasible. Therefore, we have $N_{\text{col}}(\text{He}^0 2^3\text{S}) = 6.46 \pm 1.48 \times 10^{13} \text{ cm}^{-2}$. However, the SED-constrained outflow model predicts a much larger $N_{\text{col}}(\text{He}^0 2^3\text{S})$. For the outflow model plotted in Extended Data Fig. 9 panel (b), $N_{\text{col}}(\text{He}^0 2^3\text{S}) > 10^{15} \text{ cm}^{-2}$. Alternatively, if we use the measured $N_{\text{col}}(\text{He}^0 2^3\text{S})$ to define the thickness of the outflow ($N_{\text{H}}(\text{HeI}^*)$ in Extended Data Fig. 9 panel (b)), the shielding gas would be overly thin. The transmitted SED at $N_{\text{H}}(\text{HeI}^*)$ is plotted in Extended Data Fig. 9 panel (c), in which the amount of residual high energy photons are still large enough to generate C^{3+} far more than that measured in the redshifted system.

A possible explanation for such an inconsistency is the geometry issue. Since the outflow in our objects is considered cLOSE to the very center of the quasar nucleus, where the nature (e.g. the thermal structure) of the inner accretion disk or the origin of the X-ray is not fully understood, and the assumption that the covering factor of the blueshifted BAL system is wavelength-independent may be questionable[43]. If C_{f} decreases as wavelength increases, our current measurements for $N_{\text{col}}(\text{He}^0 2^3\text{S})$ can be a significant underestimation. The true value of $N_{\text{col}}(\text{He}^0 2^3\text{S})$ may be consistent with the SED-constrained outflow thickness.

Besides the geometry issue, the metallicity, which has been found to be super-solar and varying considerably in outflows[46] may also be an explanation for the inconsistency. While the metal abundance has little effect on the ionization structure of $\text{He}^0(2^3\text{S})$, the C^{3+} region moves forward (toward the illuminated surface) when the metal abundance increases. At solar abundances, $N_{\text{H,outflow}}$ that is determined using the full development of C^{3+} region is about 3 times as large as that determined using $N_{\text{col}}(\text{He}^0 2^3\text{S})$, while for $Z = 10 Z_{\odot}$ these two values are about the same. In Extended Data Fig. 10, we plot the transmitted SED through gas of $N_{\text{H}}(\text{HeI}^*)$ for $Z = 0.1, 1, 10 Z_{\odot}$, respectively. Obviously, with increasing metallicity, the transmitted SED tends to resemble the incident SED, as expected by our inflow models.

Mass flux rate of the blueshifted BAL outflow Following the discussion of a continuous layer as the inflow model, the mass flux rate of outflow can also be expressed as

$$\begin{aligned}
\dot{M}_{\text{outflow}} &= \mu m_{\text{p}} 2\pi d_{\text{outflow}} \int_{h'} n_{\text{H}} f_{\text{f}}(h') v_{\text{out}}(h') dh' \\
&= \mu m_{\text{p}} 2\pi d_{\text{outflow}} \int_{l'} n_{\text{H}} f_{\text{f}}(l') v_{\text{out,obs}} / \cos i_{\text{out}} dl \sin i_{\text{out}} \\
&= \mu m_{\text{p}} 2\pi d_{\text{outflow}} \int_{v'_0}^{v'_1} dN_{\text{H}} / dv_{\text{out,obs}} C_{\text{f}}(v_{\text{out,obs}}) v_{\text{out,obs}} dv_{\text{out,obs}} \tan i_{\text{out}}
\end{aligned} \tag{3}$$

where h' is the height of the outflow layer at the distance d_{outflow} , l' is the length along the LOS, i_{out} is the angle between the true outflow velocity and our LOS, and v'_0 and v'_1 are the observed minimum and maximum radial velocities of the blueshifted C IV trough, respectively. As $C_{\text{f}}(v_{\text{out,obs}}) = 1$ for the blueshifted C IV BAL, we have $\dot{M}_{\text{outflow}} \approx 0.05 d_{\text{outflow}}(R_{\text{g}}) \tan i_{\text{out}} M_{\odot} \text{yr}^{-1}$ for the best inflow model, assuming the outflow structure to be axisymmetric. Though d_{outflow} can hardly be constrained by the observation, the value of d_{outflow} in units of R_{g} ($d_{\text{outflow}}(R_{\text{g}})$) is believed to be between ~ 100 and $\sim 1,000$.

9 BAL Inflow and Outflow in Emission Lines

Only when intercepting our LOS will the inflow or outflow gas be observed as redshifted or blueshifted BAL systems. However, the emission from the inflows and outflows should be detectable in any direction. Our simulation can also predict the surface emissivity (radiative energy output from unit area) for various emission lines in both of the outflows and inflows. In the outflow's emission lines, we find little variation in the emissivity within the range of distance $100 - 1,000 R_{\text{g}}$ with [O III] as the only exception, which is strongly dependent on the flows' density. The ratios between the emissivity in the inflow and that in the outflow are found to depend on the ionization state, as we expect, according to the ionization structure. For C IV the emissivity in an inflow is 3 orders of magnitude less than that in an outflow, while for Mg II the emissivity in the inflow is about 5 times larger than that in the outflow. In the case of $\text{H}\alpha$, the emissivity in the inflow is comparable to that in the outflow. Detection of the expected quasar inflows in low-ionization emission lines will be presented in a forthcoming paper.

In Supplementary Table 1, we present the equivalent widths (EWs) of various emission lines predicted for inflows and outflows. Assuming global covering factors Ω of 0.6 for inflows and 0.4 for outflows, the EWs for both outflows' and inflows' emission for $\text{H}\alpha$ are of several tens Å, which is comparable to the broad emission of typical quasars and thus supposed to be detectable. Actually, we do find the $\text{H}\alpha$ peak in J1035+1422 much wider than that in the SDSS composite[31], which could be an emission signature from outflows and inflows (Extended Data Fig. 11). The excess parts on the blue and red may be originated from the accretion disk as in a small fraction ($\sim 4\%$) of AGNs that show a 'double-peaked' profile in low-ionization broad emission lines[45]. Detailed discussion of emission lines from inflows and outflows will be presented in a companion paper.

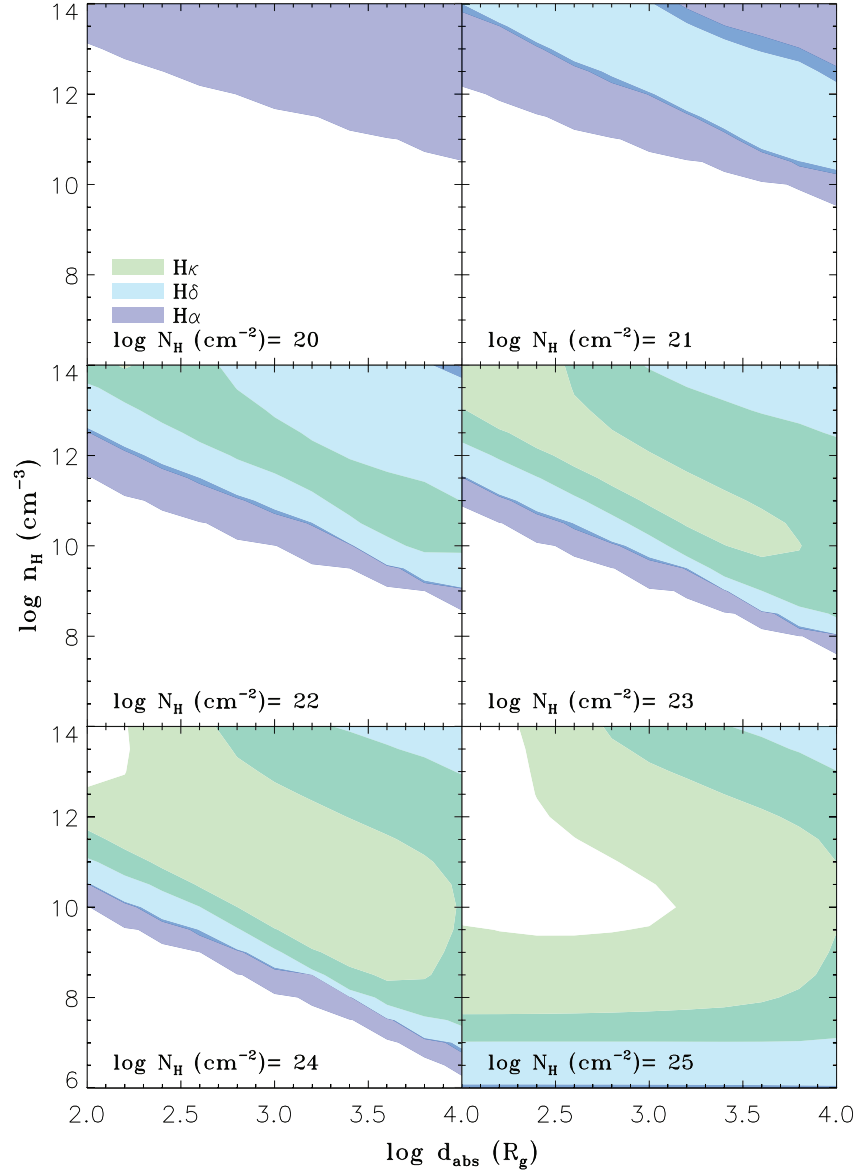
10 Data availability.

The observations discussed in this paper were mostly made using the P200 under Telescope Access Programme (TAP).

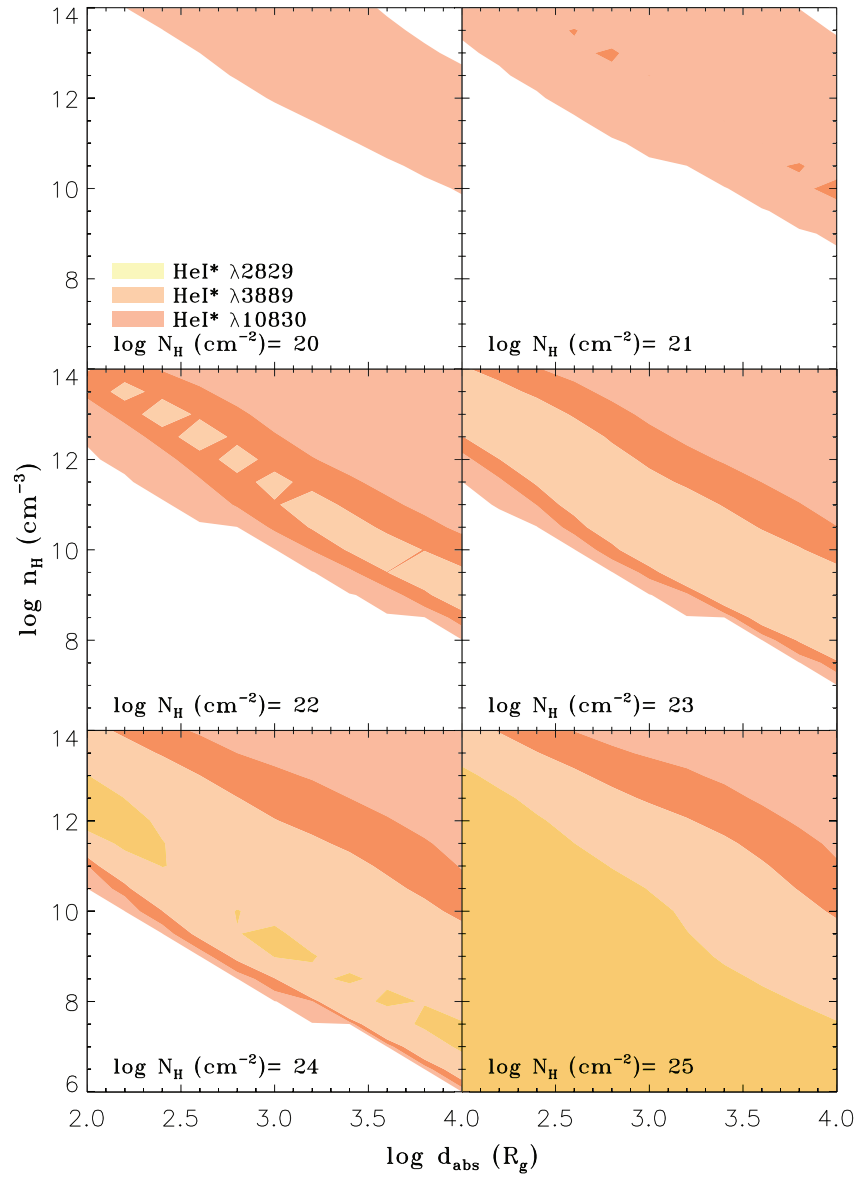
Additional references

29. Ferland, G. J., Korista, K. T., Verner, D. A., Ferguson, J. W., Kingdon, J. B., Verner, E. M. 1998. CLOUDY 90: Numerical Simulation of Plasmas and Their Spectra. *Publications of the Astronomical Society of the Pacific* 110, 761–778.
30. Cushing, M. C., Vacca, W. D., Rayner, J. T. 2004. Spextool: A Spectral Extraction Package for SpeX, a 0.8-5.5 Micron Cross-Dispersed Spectrograph. *Publications of the Astronomical Society of the Pacific* 116, 362–376.
31. Vanden Berk, D. E., and 61 colleagues 2001. Composite Quasar Spectra from the Sloan Digital Sky Survey. *The Astronomical Journal* 122, 549–564.
32. Gordon, K. D., Clayton, G. C., Misselt, K. A., Landolt, A. U., Wolff, M. J. 2003. A Quantitative Comparison of the Small Magellanic Cloud, Large Magellanic Cloud, and Milky Way Ultraviolet to Near-Infrared Extinction Curves. *The Astrophysical Journal* 594, 279–293.
33. Eracleous, M., Halpern, J. P. 1994. Doubled-peaked emission lines in active galactic nuclei. *The Astrophysical Journal Supplement Series* 90, 1–30.
34. Eracleous, M., Halpern, J. P. 2003. Completion of a Survey and Detailed Study of Double-peaked Emission Lines in Radio-loud Active Galactic Nuclei. *The Astrophysical Journal* 599, 886–908.
35. Wu, X.-B., Liu, F. K. 2004. Black Hole Mass and Accretion Rate of Active Galactic Nuclei with Double-peaked Broad Emission Lines. *The Astrophysical Journal* 614, 91–100.
36. Lewis, K. T., Eracleous, M. 2006. Black Hole Masses of Active Galaxies with Double-peaked Balmer Emission Lines. *The Astrophysical Journal* 642, 711–719.
37. Runnoe, J. C., Brotherton, M. S., Shang, Z. 2012. Updating quasar bolometric luminosity corrections. *Monthly Notices of the Royal Astronomical Society* 422, 478–493.
38. Zhang, S., Wang, H., Wang, T., Xing, F., Zhang, K., Zhou, H., Jiang, P. 2014. Outflow and Hot Dust Emission in Broad Absorption Line Quasars. *The Astrophysical Journal* 786, 42.
39. Barvainis, R. 1987. Hot dust and the near-infrared bump in the continuum spectra of quasars and active galactic nuclei. *The Astrophysical Journal* 320, 537–544.
40. Brandt, W. N., Laor, A., Wills, B. J. 2000. On the Nature of Soft X-Ray Weak Quasi-stellar Objects. *The Astrophysical Journal* 528, 637–649.
41. Green, P. J., Aldcroft, T. L., Mathur, S., Wilkes, B. J., Elvis, M. 2001. A Chandra Survey of Broad Absorption Line Quasars. *The Astrophysical Journal* 558, 109–118.
42. Gibson, R. R., and 11 colleagues 2009. A Catalog of Broad Absorption Line Quasars in Sloan Digital Sky Survey Data Release 5. *The Astrophysical Journal* 692, 758–777.
43. Shi, X.-H., Pan, X., Zhang, S.-H., Sun, L.-M., Wang, J.-G., Ji, T., Yang, C.-W., Liu, B., Jiang, N., Zhou, H.-Y. 2017. Discovery of Variable Hydrogen Balmer Absorption Lines with Inverse Decrement in PG 1411+442. *The Astrophysical Journal* 843, L14.

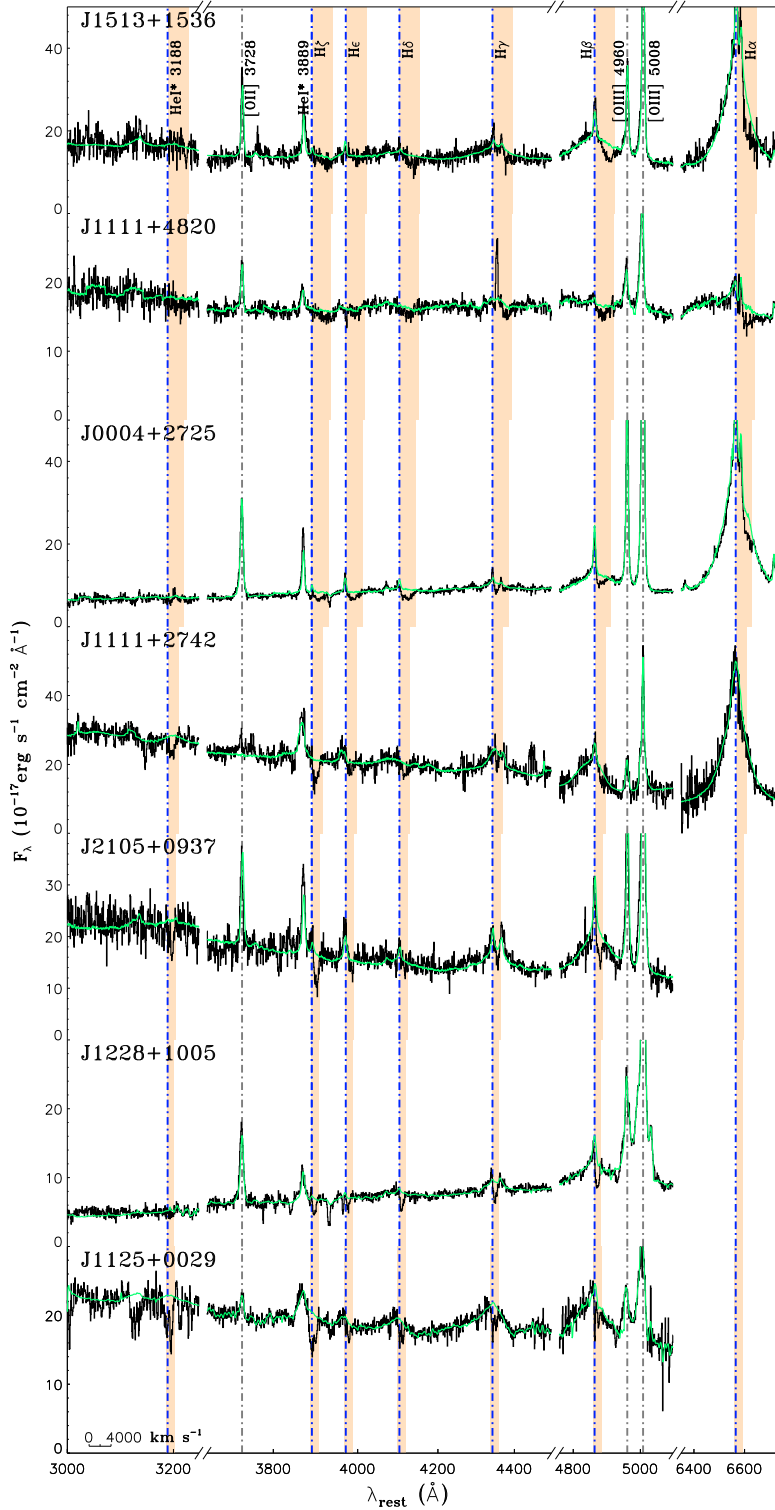
44. Glikman, E., Helfand, D. J., White, R. L. 2006. A Near-Infrared Spectral Template for Quasars. *The Astrophysical Journal* 640, 579–591.
45. Eracleous, M., Halpern, J. P., Storchi-Bergmann, T., Filippenko, A. V., Wilson, A. S., Livio, M. The ultraviolet spectra of active galaxies with double-peaked emission lines. *The Interplay Among Black Holes, Stars and ISM in Galactic Nuclei* **222**, 29–32, (2004).
46. Wang, H., Zhou, H., Yuan, W. & Wang, T. 2012. Metallicity and quasar outflows. *The Astrophysical Journal Letter* 751, 23–27.



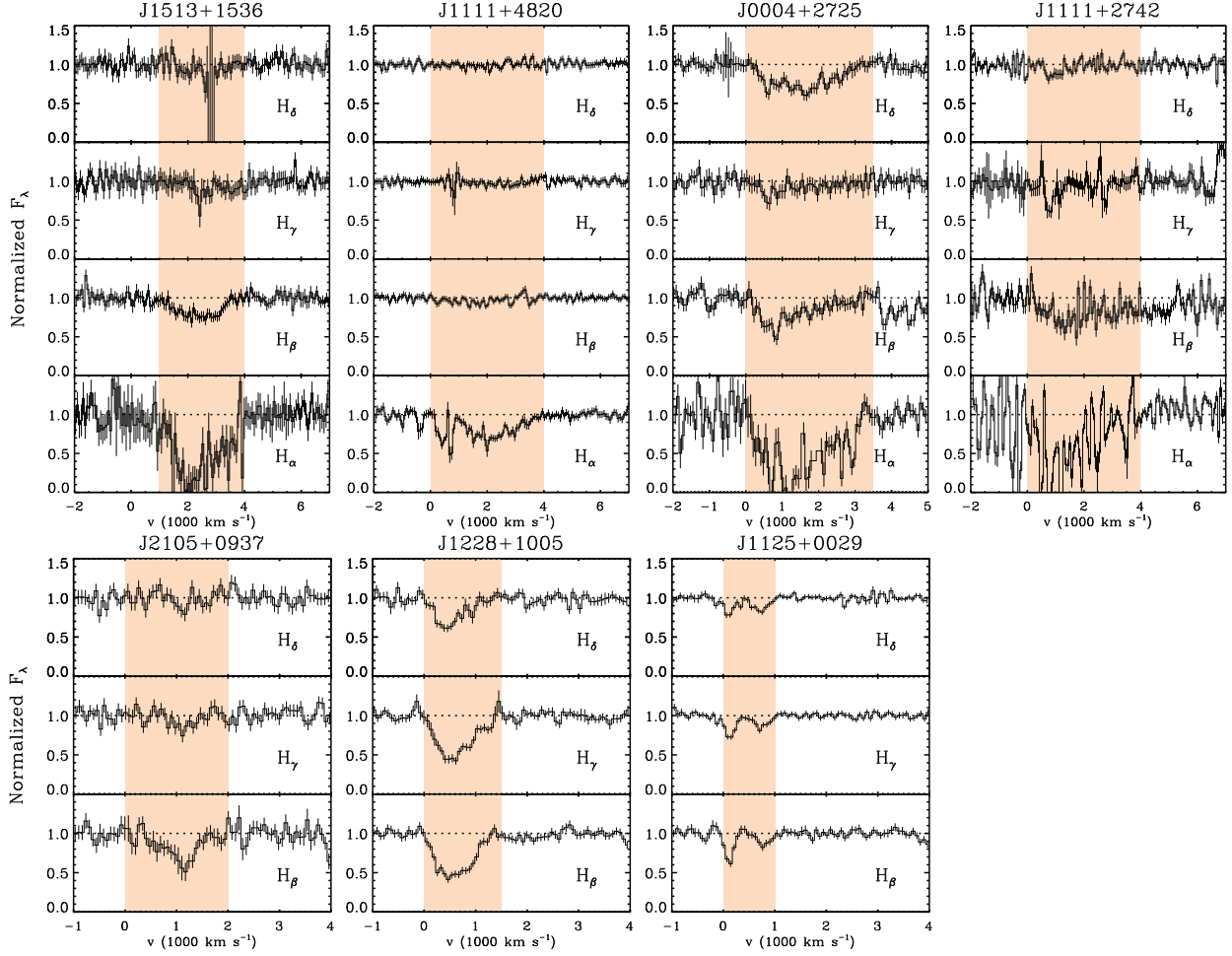
Extended Data Fig. 1: Sensitive range of the BALs in the hydrogen Balmer series H_{n+2} for gas in the vicinity of a SMBH. Assuming a black hole of $M_{\bullet} = 10^9 M_{\odot}$ accreting at an Eddington ratio of 0.1, the column densities of $H_{n=2}$ at the $n = 2$ level $N_{\text{col}}(H_{n=2}^0)$ are evaluated by photoionization simulations for gas of various density n_H , total column density N_H and distance (in units of R_g). Assuming a Gaussian velocity dispersion (FWHM = 3,000 km s $^{-1}$), a specified line would be considered to be sensitive in measuring the ionic column density as long as the optical depth is in the range of 0.05–3 at the line center. The colored area shows the sensitive range for each of the individual lines of only H α , H δ , and H κ for clarity ($\lambda_{\text{rest}} = 6,564, 4,102$ and 3,750 Å, respectively).



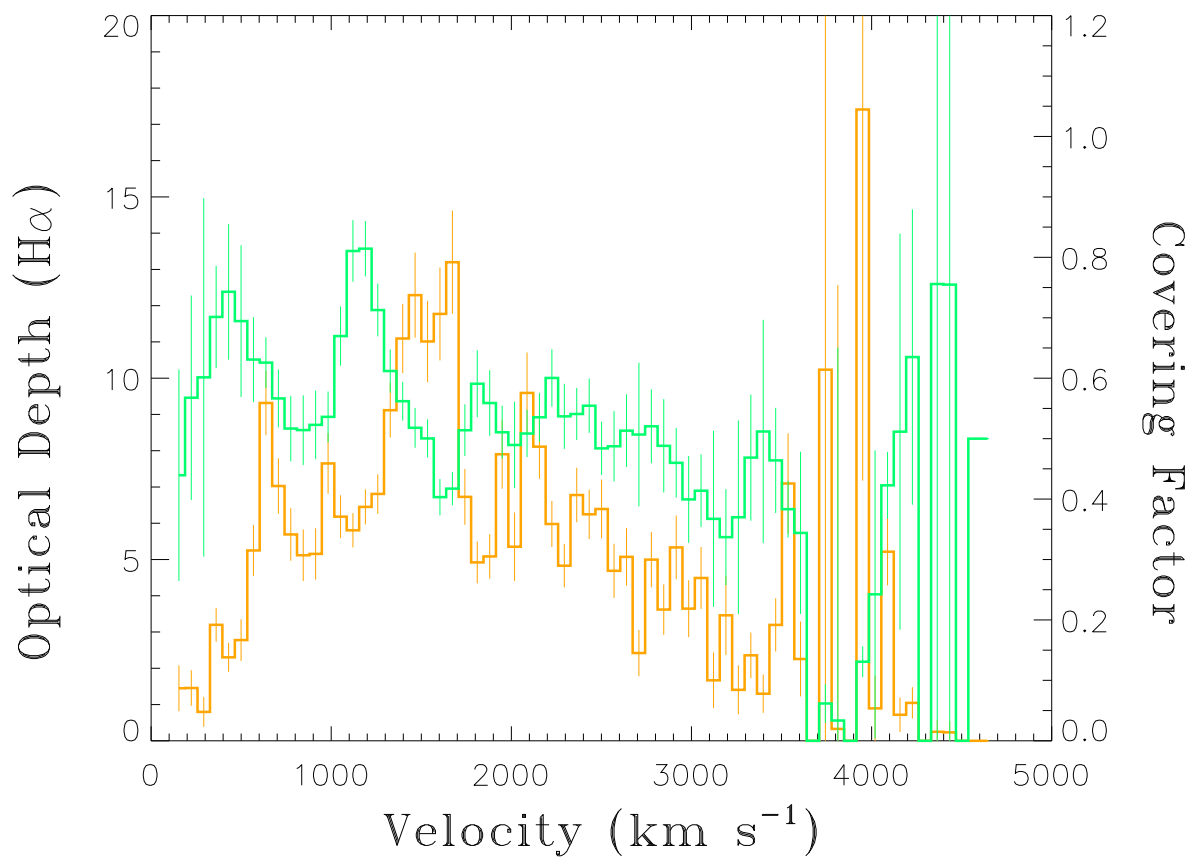
Extended Data Fig. 2: Same as Extended Data Fig. 1, but for the He I_n* BALs.



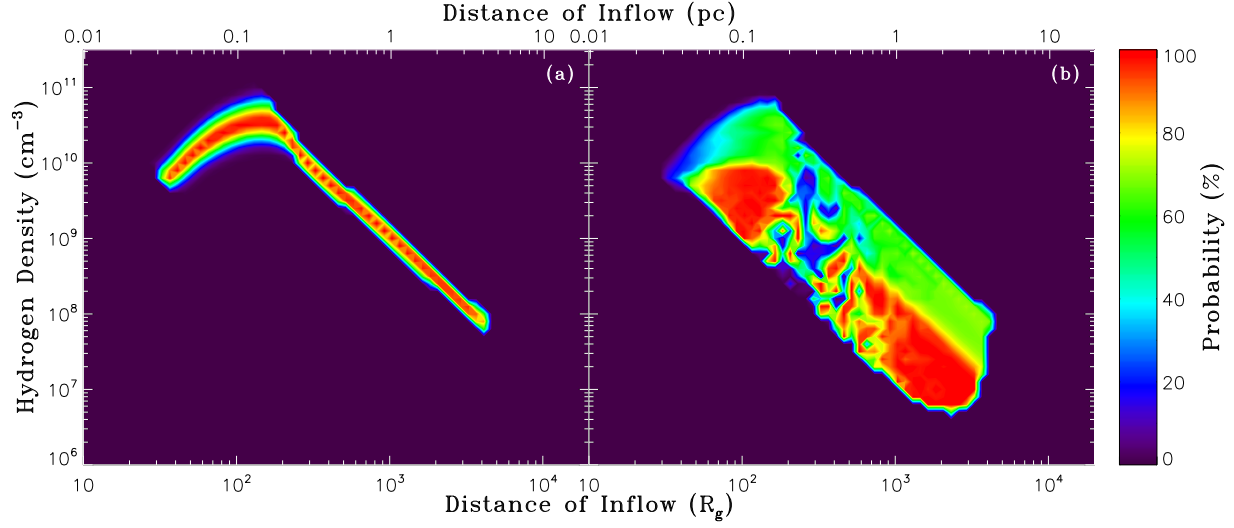
Extended Data Fig. 3: SDSS observed spectra of the remaining seven quasars of our sample with pure redshifted BALs (or mini-BALs) in the H Balmer and meta-stable He I* plotted in their rest frames. The systemic redshifts are determined from narrow emission lines including [O II] (gray dotted-dashed vertical lines). As in Figure 1 of the main text, the blue dash-dotted lines mark the rest wavelengths of the H Balmer and He I* transitions. The wavelength ranges of the absorption lines are shaded in orange.



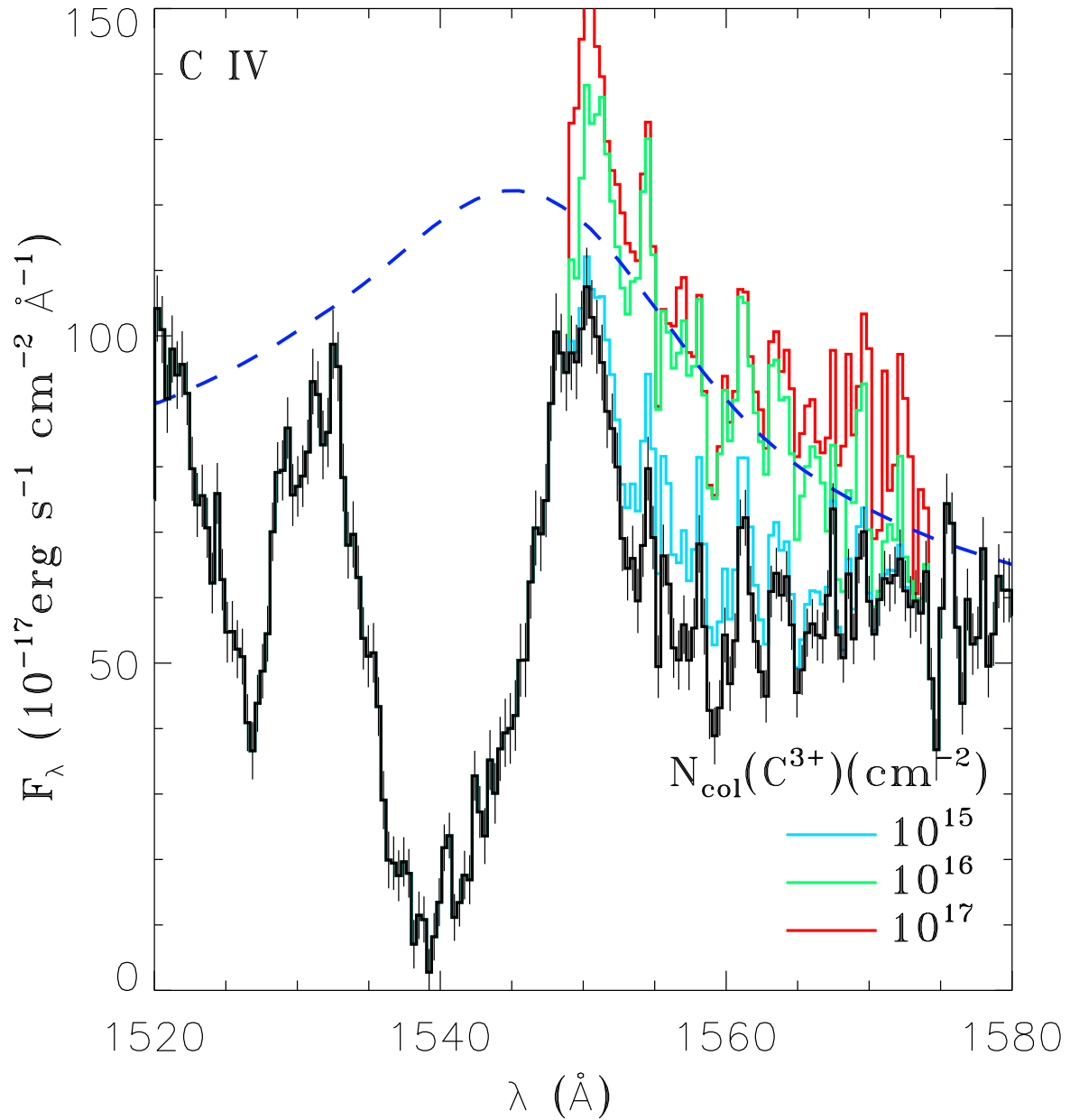
Extended Data Fig. 4: Selected Balmer absorption lines (shaded in orange) on the SDSS spectra of the seven quasars in Extended Data Fig. 3 plotted in their common velocity space. The data are normalized by the continuum after subtracting the best-fit emission line models (as for J1035+1422 in Figure 2). The upper panels show four bona fide BAL quasars with absorption troughs spanning a large range of velocities from ~ 0 to $\sim 4,000 \text{ km s}^{-1}$, significantly broader than the BAL definition criterion of $2,000 \text{ km s}^{-1}$). The absorption troughs of the remaining three quasars in the lower panels have widths $\sim 1,000 - 2,000 \text{ km s}^{-1}$ and are formally classified as ‘mini-BALs’.



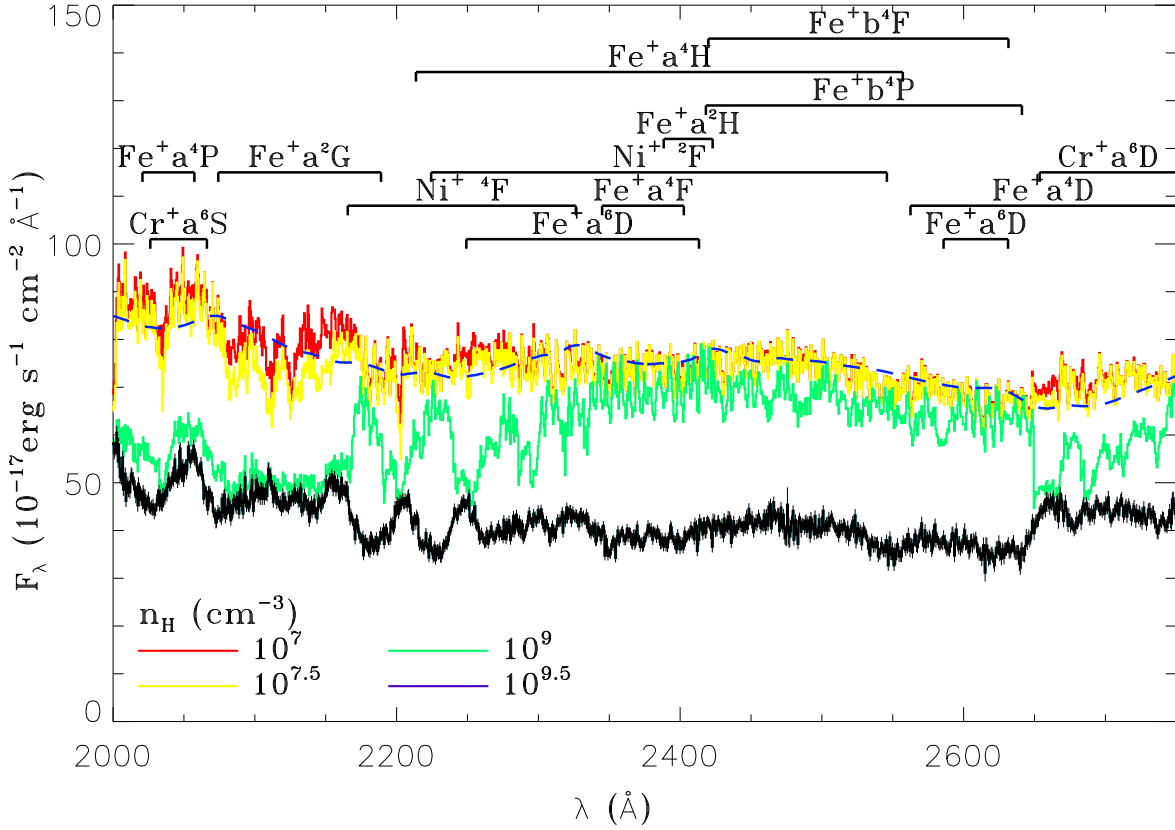
Extended Data Fig. 5: Optical depth (orange) and the covering factor (green) of the redshifted H α BAL, derived from the continuum-normalized spectrum, as a function of velocity shift with respect to the quasar’s rest-frame.



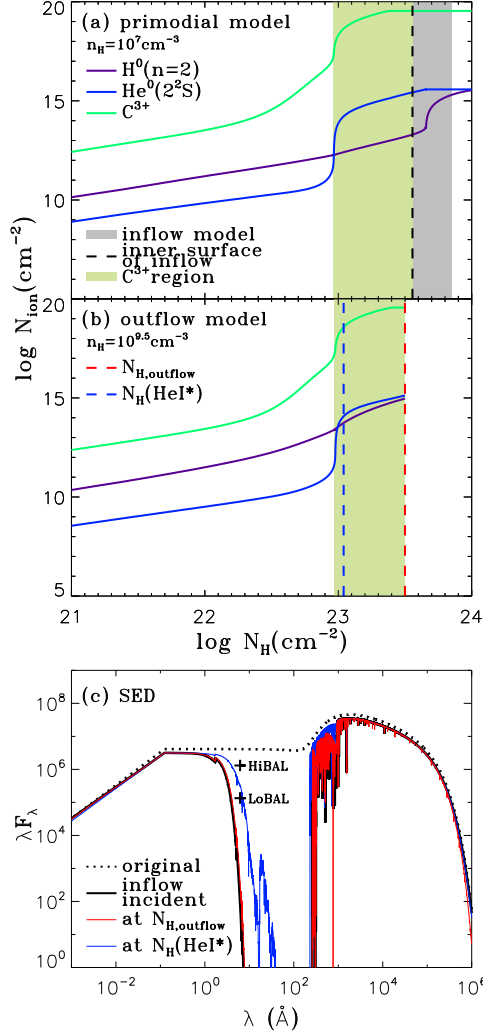
Extended Data Fig. 6: Probability density distribution in the parameter space of the total hydrogen density n_{H} and the distance from the central engine d_{inflow} for the inflow models (see also Figure 3 of the main text). In panel (a) the simplest primordial models are applied, and the redshifted H I Balmer and He I* BALs are employed to evaluate the probability density. However, the highly probable models predict much higher column densities of C^{3+} ions $N_{\text{col}}(\text{C}_{\text{ground}}^{3+})$ than that evaluated from the redshifted C IV BAL trough. To resolve this problem, only the region beyond the C^{3+} region (post C^{3+} region in short) in the primordial models is used to describe the inflow gas, and probability density is recalculated by including C IV. The results of these refined model calculations are displayed in panel (b), where the probability density shows two peaks around $n_{\text{H}} \approx 10^7 \text{ cm}^{-3}$ and $d_{\text{inflow}} \approx 2,000 R_{\text{g}}$, and $n_{\text{H}} \approx 10^{9.5} \text{ cm}^{-3}$ and $d_{\text{inflow}} \approx 100 R_{\text{g}}$, respectively.



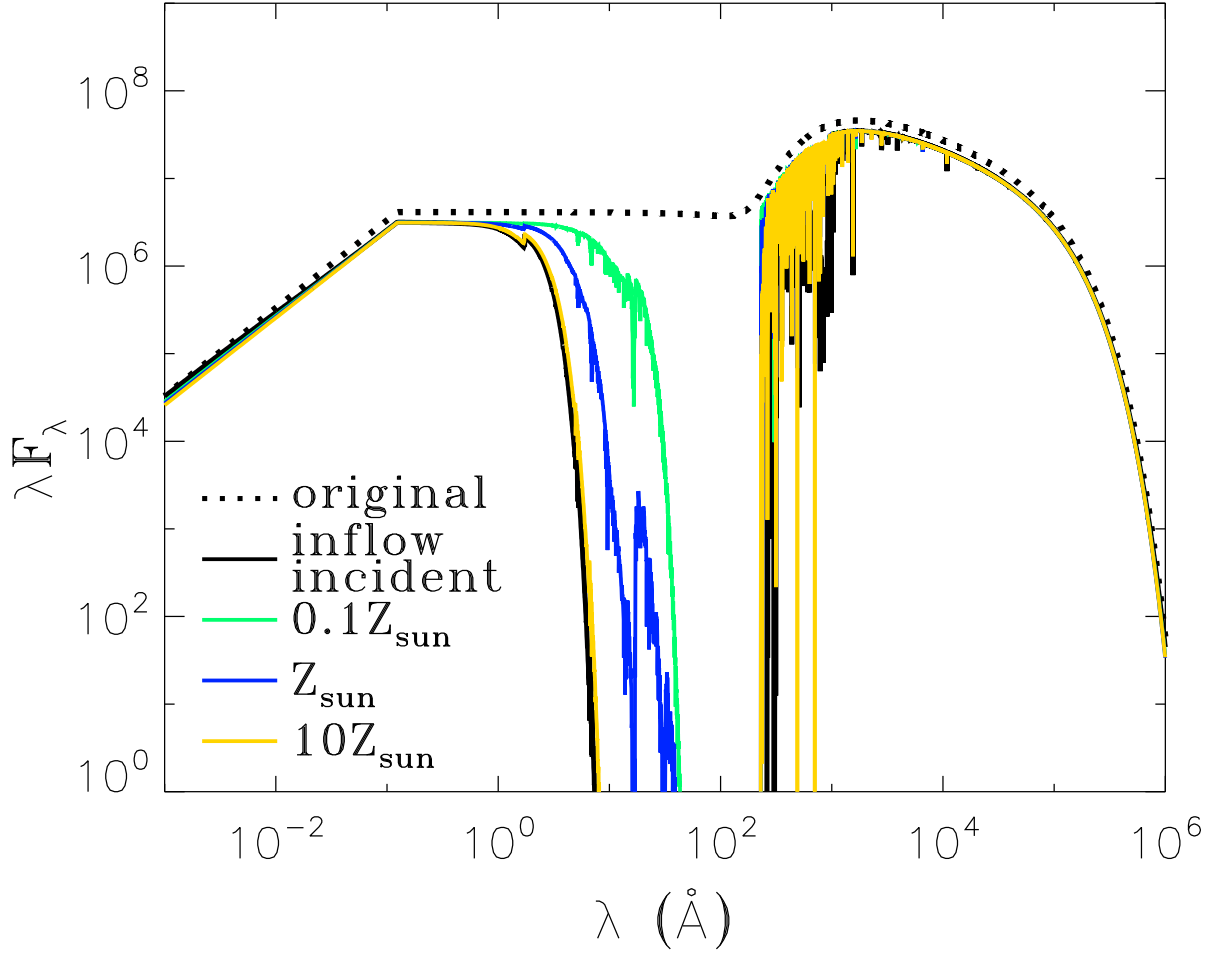
Extended Data Fig. 7: Recovered spectra of C IV corrected for the redshifted absorption assuming C^{3+} ion column densities of $\log N_{\text{col}}(C_{\text{ground}}^{3+})(\text{cm}^{-2}) = 15$ (cyan), 16 (green) and 17 (red) in the quasar’s rest-frame. Compared to the best-fit SDSS composite spectrum (blue dashed line), the recovered flux is much too weak for the absorption with $\log N_{\text{col}}(C_{\text{ground}}^{3+})(\text{cm}^{-2}) = 15$, while it is too high showing two extra deceptive peaks at ~ 1550 and 1570 \AA for the absorption with $\log N_{\text{col}}(C_{\text{ground}}^{3+})(\text{cm}^{-2}) = 17$. The absorption model with $\log N_{\text{col}}(C_{\text{ground}}^{3+})(\text{cm}^{-2}) \approx 16$ predicts unabsorbed flux reasonably consistent with the composite spectrum, and is thus adopted.



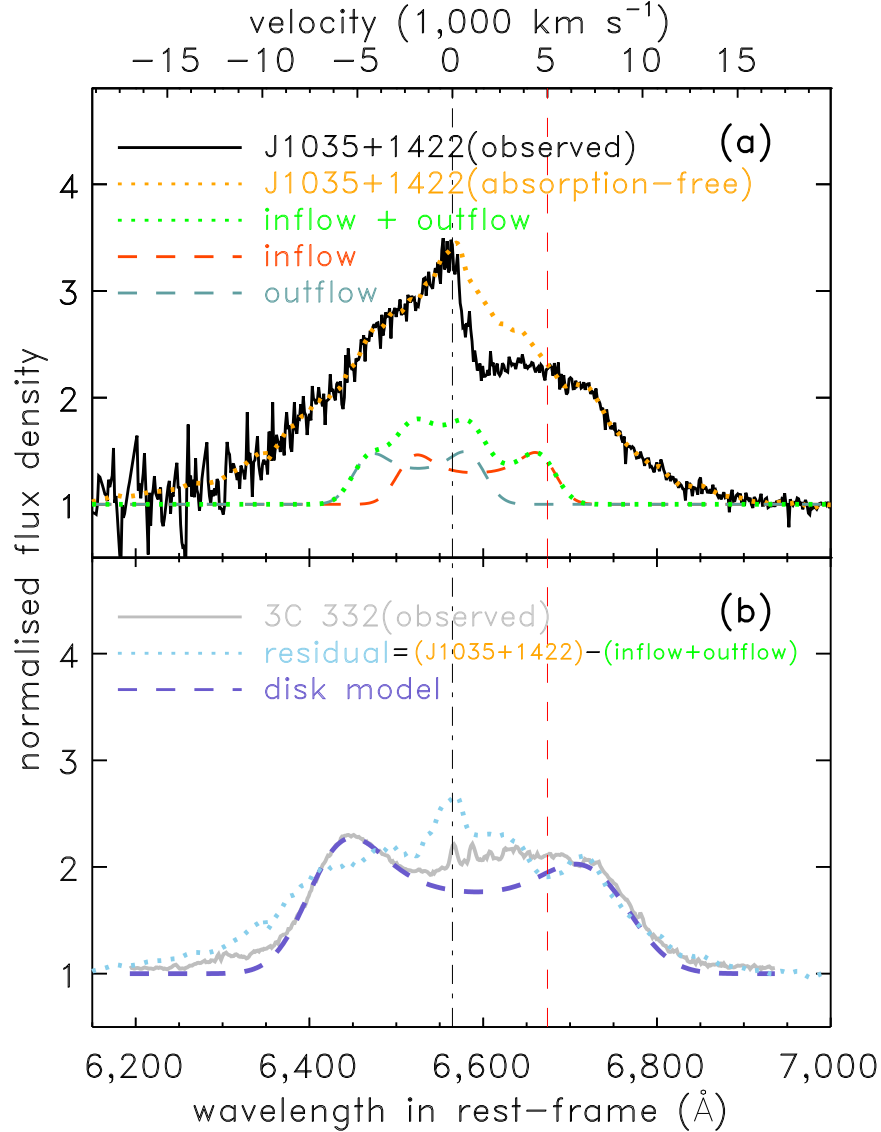
Extended Data Fig. 8: Absorption-corrected UV Fe II spectra between 2000 and 2750 \AA for the post- C^{3+} inflow models with $\log n_H(\text{cm}^{-3}) = 7$ (red), 7.5 (yellow), 9 (green), and 9.5 (violet) in the high ‘probability’ zone of Extended Data Fig. 6 panel (b). Compared with the best-fit composite (blue dashed), the models with higher densities can be clearly ruled out.



Extended Data Fig. 9: Photo-ionization model for the inflow and outflow. Panel (a) shows the ionization structure of a primordial model with $n_H = 10^7 \text{ cm}^{-3}$ and $U = 10^{0.5}$, which is directly illuminated by the central continuum source of the quasar. If integrated from the illuminated surface, the model with $N_{\text{col}}(\text{H}_{n=2}^0)$ and $N_{\text{col}}(\text{He}^0 2^3\text{S})$ comparable to the measurements predicts $N_{\text{col}}(\text{C}_{\text{ground}}^{3+}) > 10^{19} \text{ cm}^{-2}$, far from the estimated $N_{\text{col}}(\text{C}_{\text{ground}}^{3+})$ in the redshifted BAL. An alternative solution is that the inflow in fact corresponds to the gas behind the C^{3+} region (the light green area where C^{3+} and other high-ionization ions dominate), which is shown as the grey area. In such a picture, the outflow is suggested to play an equivalent role as the C^{3+} region in panel (a) in eliminating high energy ionizing photons. In panel (b), we plot the ionization structure for the outflow with $n_H = 10^{9.5} \text{ cm}^{-3}$ and $U = 10^{0.5}$. The requirement for the transmitted radiation (which should have the same SED as the incident radiation on inflow) could constrain the thickness of outflow model. The outer surface of this model (red dashed line) highly coincides the extension of the C^{3+} region. However, $N_{\text{col}}(\text{He}^0 2^3\text{S})$ measured using the blueshifted $\text{He I}^* \lambda 10830$ defines a thinner outflow gas (see the blue dashed line) if we assume the covering factor C_f is wavelength-independent. In panel (c), we plot the transmitted SEDs through the SED-constrained outflow and the $N_{\text{col}}(\text{He}^0 2^3\text{S})$ -defined outflow. The former (red) naturally consists with the incident SED for the inflow model, while the latter (blue) shows considerable excess in soft X-ray which would result in a much larger $N_{\text{col}}(\text{C}_{\text{ground}}^{3+})$ in the inflow than the measurement.



Extended Data Fig. 10: Transmitted SEDs through a $N_{\text{col}}(\text{He}^0 2^3\text{S})$ -defined outflow model with $n_{\text{H}} = 10^{9.5} \text{ cm}^{-3}$, $U = 10^{0.5}$ and different metallicities. The SED sensitively depends on the metallicity. As the metallicity increases from solar to $10 Z_{\odot}$, the transmitted SED seems to match the incident SED required by the inflow model, suggesting that a metal-rich outflow model could explain the measurement in both the redshifted and blueshifted BAL systems.



Extended Data Fig. 11: Upper panel: Observed (dark gray solid line) and the absorption-corrected (orange dotted line) broad H α emission line spectra of J1035+1422 normalized to the continuum. Over-plotted for comparison are the predicted H α emission lines by the photo-ionization models from the inflow (red dashed line), the outflow (blue dashed line), and the total as a combination of the two (green dotted line) (assuming a covering factor of 0.5 ($\Omega_i = \Omega_o = 0.5$ in Supplementary Table) and a radial velocity 5,000 km s⁻¹ for both the inflow and outflow.) Clearly, the observed H α is significantly stronger than the model prediction. This may be due to the over-simplicity of the models, in which a much broader velocity range is missing. Alternatively and more likely, the excess H α flux may be contributed from the accretion disk. The lower panel shows the residual line profile (cyan dotted line; the zigzag shape is caused by the oversimplified model assumption of a single velocity instead of a large velocity gradient in reality), which largely resembles the H α line observed in the well-studied disk emitting quasar 3C 332[45] (gray solid line). Note that 3C 332 shows a significant excess component with respect to the best-fit disk line model (violet dashed line), which is redshifted with a velocity range $\sim 0 - 5,000$ km s⁻¹. This is reminiscent of the redshifted H α BAL found in J1035+1422 here, suggestive of an interesting possibility that this excess H α emission might originate from inflows in 3C 332.

Supplementary Table 1. Predicted emission lines from the outflow and inflow of J1035+1422 in comparison with the averaged BEL EWs of quasars.

line	outflow [†] Å	inflow [†] Å	averaged BEL Å	reference
C IV $\lambda\lambda$ 1548, 1550	65 – 69 Ω_o	0.051 Ω_i	23.78	[31]
Al III $\lambda\lambda$ 1855, 1863	2.3 Ω_o	0.81 Ω_i	0.40	[31]
Mg II $\lambda\lambda$ 2796, 2803	5.0 Ω_o	32 Ω_i	32.28	[31]
H α	140 Ω_o	150 Ω_i	194.52	[31]
He I* λ 10830	53 – 61 Ω_o	15 Ω_i	36	[44]